

1 **Polarity and direction dependence of energetic cross-frontal eddy transport in the Southern**
2 **Ocean's Pacific sector**

3 Huimin WANG¹, Lingqiao CHENG^{1,5*}, Erik BEHRENS², Zhuang CHEN^{1,4,5}, Jennifer DEVINE³, Guoping
4 ZHU^{4,5,6,7}

5 ¹*College of Oceanography and Ecological Science, Shanghai Ocean University, Shanghai, China*

6 ²*Earth Sciences New Zealand, Wellington, New Zealand*

7 ³*Earth Sciences New Zealand, Nelson, New Zealand*

8 ⁴*College of Marine Living Resource Sciences and Management, Shanghai Ocean University, Shanghai, China*

9 ⁵*Center for Polar Research, Shanghai Ocean University, Shanghai, China*

10 ⁶*Polar Marine Ecosystem Group, The Key Laboratory of Sustainable Exploitation of Oceanic Fisheries Resources,*
11 *Ministry of Education, Shanghai, China*

12 ⁷*International Research Center for Marine Biosciences at Shanghai Ocean University, Ministry of Science and*
13 *Technology, China*

14 * **Correspondence:** Lingqiao Cheng (lqcheng@shou.edu.cn)

15 **Abstract:**

16 Mesoscale eddies play a critical role in mediating meridional transport across the Antarctic Circumpolar Current
17 (ACC), yet the dynamics of cross-frontal eddies (CFEs) and their energy exchanges with frontal jets remain
18 inadequately quantified. This study presents a systematic analysis of CFE characteristics, kinetic energy evolution,
19 and thermohaline transport effects in the Pacific sector of the Southern Ocean, utilizing 23 years (2000–2022) of
20 satellite altimetry and Argo float data. Our results reveal a fundamental polarity- and direction-dependent
21 asymmetry in CFE dynamics. Equatorward-propagating cyclonic eddies (CEs) dominate CFE activity, followed by
22 poleward-moving anticyclonic eddies (AEs). These dominant CFE types exhibit superior energetic characteristics,
23 including significantly higher eddy kinetic energy (*EKE*) and stronger nonlinearity compared to their counterparts.
24 Complete CFEs experience polarity- and direction-selective energy gains during frontal crossing, with equatorward
25 CEs and poleward AEs extracting energy from eastward frontal jets, while their counterparts lose energy. This
26 energization mechanism has intensified over the past two decades, with both polarity CFEs showing substantial
27 *EKE* increases that substantially exceed previous basin-scale estimates. Hydrographic analysis demonstrates that
28 CEs and AEs transport distinct water masses across frontal boundaries, creating sharp thermohaline contrasts within
29 interfrontal zones. Our findings establish CFEs as crucial regulators that buffer wind- and warming- induced
30 baroclinicity increases through compensatory heat transport, thereby maintaining the Southern Ocean's thermal
31 equilibrium and modulating the ACC's response to external forcing in a changing climate.

32 **Keywords:** Cross-frontal eddies; Eddy kinetic energy; Meridional transport; Antarctic Circumpolar Current; the
33 Pacific sector of the Southern Ocean

34 **1 Introduction**

35 Mesoscale eddies are ubiquitous in the Southern Ocean (SO), play a vital role in the zonal and meridional
36 transport of quantities including heat and momentum across the Antarctic Circumpolar Current (ACC), and also
37 influence the uptake of heat and carbon dioxide from the atmosphere (Moreau et al., 2017; Patel et al., 2019; Sallée
38 et al., 2008; Sokolov and Rintoul, 2007) and the transport and connectivity of marine species (e.g., Duan et al.,
39 2020; Zhu et al., 2025). The ACC comprises multiple zonal fronts, where oceanic jets exit. Here, a front refers to a
40 boundary between distinct water masses, characterized by strong horizontal density gradients, while a jet denotes
41 the narrow, swift current that flows along the axis of such a front. Together, they form the dynamic core of the
42 ACC. At these fronts, mesoscale activity is enhanced, with higher eddy kinetic energy (*EKE*) and more frequent
43 eddy generation and dissipation (Barthel et al., 2017; Gille, 1994; Hughes, 1995; Hughes and Ash, 2001; Morrow
44 et al., 1994; Sokolov and Rintoul, 2002). In turn, eddies impact the fronts' structure, intensity, and location. For
45 instance, eddies may accelerate the jets, and cyclonic (anticyclonic) eddies cause the equatorward (poleward)
46 deviation of frontal meanders in some cases (Chapman et al., 2020; Duan et al., 2016; Frenger et al., 2015; Sprintall,
47 2003). These interactions between mesoscale eddies and oceanic fronts can shape local thermohaline structures,
48 exert profound influences on large-scale circulation and vertical flux processes. They also have tremendous
49 implications for the redistribution and survival of marine species and the stability of the climate system.

50 In the SO, the transition from the warm subtropical waters to the cold Antarctic waters is not smooth but
51 concentrated along a series of fronts (Orsi et al., 1995; Belkin and Gordon, 1996), often corresponding to the
52 locations of narrow, high-speed currents known as “jets” (Sokolov and Rintoul, 2002, 2007). These fronts delineate
53 the boundaries of distinct water masses, each with unique environmental characteristics (Orsi et al., 1995). The
54 existence of fronts hinders meridional exchanges of heat and tracers (Chapman and Sallée, 2017; Naveira Garabato
55 et al., 2011; Thompson and Sallée, 2012). At the same time, eddies enable cross-frontal transport and serve as
56 primary carriers for meridional water mass properties, including heat (De Szoeke and Levine, 1981; Foppert et al.,
57 2017). Cross-frontal eddies (CFEs) must overcome intense geostrophic shear to achieve material transport and
58 render their dynamical contributions to meridional transport, which is significantly more pronounced compared to
59 other eddy types (Thompson and Sallée, 2012).

60 Eddies' capability of trapping materials and achieving long-distance cross-frontal transport helps in mitigating
61 sharp meridional hydrographic gradients, facilitating new water formation and carbon transport, and also enhancing
62 subsurface temperature extremes in the SO. Holte et al. (2013) presented that cross-frontal exchanges by eddies can
63 penetrate strong potential vorticity gradients associated with the Subantarctic Front (SAF) and facilitate the

64 downstream evolution of Subantarctic Mode Water by transporting cold, low-salinity water across the ACC from
65 the Polar Front Zone (Holte et al., 2013). In a study of a cold eddy in the southwest Indian Ocean, Swart et al.
66 (2008) found that the eddy displaced temperature and salinity anomalies by 1.5° towards lower latitudes. This
67 single eddy contributed 2.5% of the annual northward flux of Antarctic Surface Water in the southwest Indian
68 sector (Swart et al., 2008). In addition, eddies induce carbon transport across the ACC, which alters the carbon
69 properties and budget of the Subantarctic Zone waters (Moreau et al., 2017). Patel et al. (2019) proposed that about
70 21% of the heat transported across the SAF to the Subantarctic Zone south of Tasmania is achieved by cyclonic
71 eddies. He et al. (2023) demonstrated that nearly half of the subsurface temperature extremes in the Southern Ocean
72 occur within eddies, with cross-frontal eddies (CFEs) generating extremely high-temperature events on the cold
73 side of the ACC and extremely low-temperature events on the warm side. These extremes eventually impact marine
74 organisms and ecosystems. For instance, *Electrona carlsbergi* in the high-latitude Antarctic region may be
75 transported across the fronts from the Argentine Basin by the poleward eddy activity (Saunders et al., 2017; Zhu et
76 al., 2025).

77 Eddies in the SO can moderate the ACC's response to surface wind forcing changes, namely the "eddy
78 saturation" hypothesis (Hallberg and Gnanadesikan, 2001, 2006; Straub, 1993). Reanalysis of data since 1972 show
79 an increasing trend in wind stress (associated with a positive trend of Southern Annular Mode) over the Pacific
80 sector that dominates the basin-wide wind stress variability, driving enhanced eddy activity responses in this sector,
81 with *EKE* intensifying at a rate of $14.9 \pm 4.1 \text{ m}^4 \text{ s}^{-2}$ per decade (Duan et al., 2016; Hogg et al., 2015; Menna et al.,
82 2020; Morrow et al., 2010). Recent work by Zhang et al. (2021) demonstrates that *EKE* intensification is not
83 spatially homogeneous in the SO but concentrated south of New Zealand and downstream of the Campbell Plateau
84 in the Pacific sector. This localized enhancement likely stems from the release of available potential energy stored
85 in tilted isopycnals, thus acting to moderate the eastward flow in the ACC, which has significantly intensified
86 between 48°S and 58°S mainly due to buoyancy forcing (Shi et al., 2021). Mesoscale energy gain from mean
87 flows is achieved through baroclinic (primary) and barotropic (secondary) pathways (Fu et al., 2023). Regarding
88 topographic effects, previous studies have established that interactions between ACC and seafloor topography
89 intensify oceanic eddy mixing by enhancing downstream baroclinic shear. This process enhances eddy generation
90 and increases *EKE* downstream of major topographic features (Frenger et al., 2015; Morrow et al., 1992; Park et al.,
91 1993; Thompson and Sallée, 2012). Consequently, ACC frontal jets with strong geostrophic characteristics
92 experience mesoscale eddy modulation near prominent topographies (Kim and Orsi, 2014; Thompson et al., 2010).

93 Despite extensive research on basin-scale *EKE* modulations and case studies of CFE transport, and the

94 well-established asymmetric eddy distribution on both sides of the ocean fronts, fundamental questions remain
95 regarding how eddy-jet interactions vary based on eddy characteristics and directional approach in the SO.
96 Specifically, it is essential to understand: (1) the polarity and direction preferences of CFEs during frontal crossing;
97 (2) the magnitude and pattern of kinetic energy change within eddies following frontal crossing; (3) the resultant
98 hydrographic property redistribution achieved by CFEs in the interfrontal zones. Motivated by these research gaps,
99 we conducted a systematic assessment of cross-frontal mesoscale eddies in the Pacific sector to elucidate their role
100 in regional ocean dynamics and hydrographic redistribution. Utilizing 23 years (2000–2022) of satellite altimetry
101 data, we characterize the spatiotemporal variability, *EKE* patterns, and eddy-jet interactions of CFEs in the Pacific
102 sector. We complement these analyses with Argo (Array for Real-time Geostrophic Oceanography) float profiles to
103 quantify normalized hydrographic differences between cyclonic and anticyclonic eddies within the interfrontal
104 zones. These approaches aim to improve our understanding of the dynamic characteristics of CFEs and their role in
105 mediating meridional transport across the ACC in this sector.

106 **2 Data and methods**

107 **2.1 Data**

108 This study focuses on the SO's Pacific sector in the range of 150°E–110°W, 35°S–80°S. Prominent
109 topographic features within this region include the Campbell Plateau, Pacific-Antarctic Ridge, Eltanin Fracture
110 Zone, and Udintsev Fracture Zone (Figure 1). We utilized the gridded satellite altimeter data for eddy detection and
111 tracking. This dataset is merged from multiple satellites and provided by the Copernicus Marine Service as the
112 CMEMS all-satellite L4 SLA product, SEA LEVEL_GLO_PHY_L4_MY_008_047 (Copernicus Marine Service,
113 2024). The data were accessed/downloaded on 18 December 2025 from the Copernicus Marine Service Information
114 (DOI: <https://doi.org/10.48670/moi-00148>). It includes daily Sea Level Anomaly (*SLA*) and sea surface geostrophic
115 velocity anomalies (u' , v') data during 2000–2022 with a spatial resolution of $0.125^\circ \times 0.125^\circ$. The *SLA*
116 represents the sea surface height anomaly relative to the mean sea surface from 1993 to 2012. The
117 corresponding geostrophic velocity anomalies (u' , v') are derived from *SLA* based on the geostrophic
118 balance (Pujol and Grassi, 2025).

119 The geographical positions of the ACC's fronts and boundaries used in this study are from the synthesis of
120 Park et al. (2019). This dataset provides the most updated mapping of the ACC frontal system and its associated
121 boundaries, derived from satellite altimetry and independently validated against extensive subsurface observations,
122 including Argo float profiles (2001–2017) and dedicated CTD surveys (2016–2017). As shown in Figure 1, the
123 dataset defines five major streamlines from north to south: the Northern Boundary (NB), the Subantarctic Front
124 (SAF), the Polar Front (PF), the Southern ACC Front (SACCF), and the Southern Boundary (SB). Specifically, the
125 NB represents the northern dynamical limit of the ACC and coincides with the northern expression of the
126 Subantarctic Front system (SAF-N) in this region. The SAF, PF, and SACCF correspond to the core frontal jets.

127 Furthermore, a total of 1094 quality-controlled Argo profiles (0–2000 m; <https://argo.ucsd.edu/data/>) located
128 within detected eddies were utilized to analyze the internal thermohaline structure of cyclonic (CEs) and
129 anticyclonic eddies (AEs). The potential temperature (θ) and salinity (S) within each eddy were normalized radially
130 by binning profiles according to their relative distance from the eddy center (normalized by the eddy radius, R), at
131 an average interval of $0.03R$. Owing to limited spatial coverage, profiles from the SB-SACCF zone and areas south
132 of the SB were excluded. Consequently, the analysis focused on the northern inter-frontal zones of SAF-NB,
133 PF-SAF, and SACCF-PF, which contained 400, 150, and 252 profiles, respectively. Furthermore, temporal
134 variability (e.g., interannual and seasonal) was not considered in this composite analysis due to the uneven
135 distribution of profiles over time.

136 2.2 Eddy detection, tracking and CFE categorization

137 We combined the Okubo-Weiss (OW) parameter method with the outermost closed contour of *SLA* to detect
 138 eddies. As a widely used eddy detection method, the OW parameter method was developed based on flow field
 139 deformation by high vorticity or high strain (Okubo, 1970; Weiss, 1991). The OW parameter is defined as:

$$140 \quad W = s_n^2 + s_s^2 - \omega^2, \quad (2)$$

141 where $s_n = \frac{\partial u'}{\partial x} - \frac{\partial v'}{\partial y}$ and $s_s = \frac{\partial v'}{\partial x} + \frac{\partial u'}{\partial y}$ are the normal and shear components of strain, respectively, and

142 $\omega = \frac{\partial v'}{\partial x} - \frac{\partial u'}{\partial y}$ is the relative vorticity of the flow. The sign of W determines a region to be strain-dominated ($W > 0$)

143 or vorticity-dominated ($W < 0$). Eddies are highly vorticity-dominated circulations, thus corresponding to coherent
 144 negative- W areas (for both CEs and AEs), and the negative W must be larger than that for the background field
 145 (Henson and Thomas, 2008).

146 To identify physically consistent eddy boundaries, we adopt the hybrid geometric–physical approach validated
 147 by Saraceno and Provost (2012), which avoids common biases associated with fixed W thresholds. A threshold of
 148 $W < -0.2 \sigma_w$ is often used to delineate eddy boundaries, with σ_w being the standard deviation of W over the entire
 149 region (e.g., Henson and Thomas, 2008; Isern-Fontanet et al., 2006; Frenger et al., 2015). However, this method
 150 can underestimate eddy area in certain regions (Matsuoka et al., 2016) and misidentify meanders as eddies in
 151 energetic frontal zones (Saraceno and Provost, 2012). Our approach proceeds as follows: after detecting the eddy
 152 center using the OW-based method, we identify the outermost closed *SLA* contour that encloses this point. This
 153 contour defines the eddy boundary, and the center was then recalculated as its geometric centroid. Eddy radius was
 154 computed as the radius of a circle of equivalent area, and eddy amplitude is the absolute *SLA* difference between
 155 the center and along the contour.

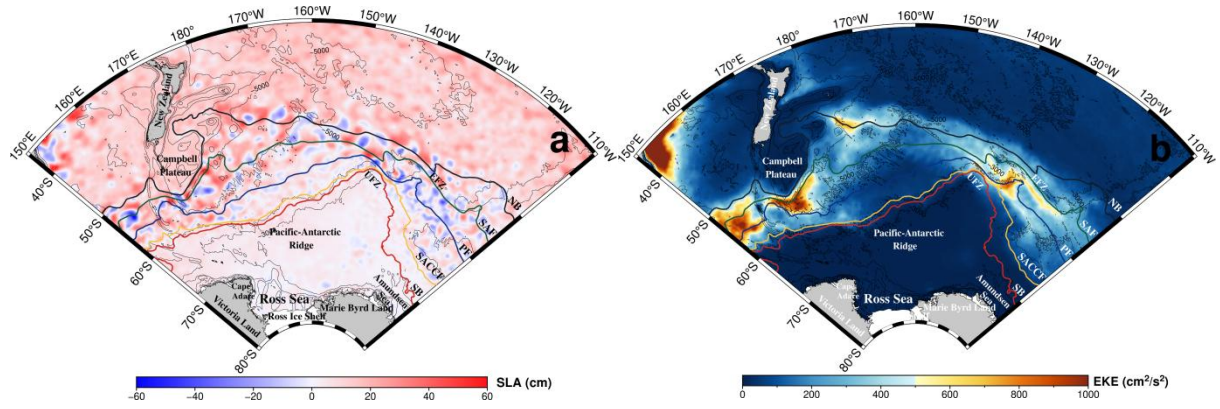
156 For eddy tracking, the algorithm identifies eddies at time $t+1$ that meet the following criteria relative to time t :
 157 (1) minimal centroid distance, (2) identical polarity (i.e., rotation direction), and (3) the minimum radius variation.
 158 If no eddy at $t+1$ satisfies these proximity thresholds for a given eddy at t , the eddy is considered dissipated.
 159 Conversely, if an eddy detected at $t+1$ does not match any eddy at t , it is classified as a newly generated eddy.

160 To ensure statistical robustness, our analysis focused exclusively on significant mesoscale eddies, which were
 161 defined as well-resolved, energetic eddies with sufficient temporal coherence. Eddies meeting all of the following
 162 criteria were retained as the core dataset for subsequent analyses: (1) radius > 30 km; (2) amplitude > 5 cm; and (3)
 163 lifespan > 14 days.

164 The *EKE* was computed from geostrophic velocity anomalies using the equation $EKE=(u^2+v^2)/2$. In this
 165 study, except for Figure 1, all analyses of *EKE* variation during cross-frontal processes were based on the total *EKE*
 166 within each eddy interior (EKE_T) for better tracking *EKE* changes in specific eddies, calculated as $EKE_T =$
 167 $\sum_{i=1}^N EKE_i \cdot ds$, where EKE_i is the *EKE* for grid i , N is the grid amount within an eddy, and ds is the grid area. The
 168 eddy nonlinearity parameter (β) was computed based on $\beta = U/C$, where U is the maximum circum-average
 169 geostrophic velocity within the eddy, and C represents the eddy's transporting speed (Chelton et al., 2011). The
 170 eddy is nonlinear when $\beta > 1$, indicating the presence of trapped fluid parcels advected with the eddy movement.

171 While climatological fronts define the ACC's mean structure (Park et al., 2019), their positions exhibit
 172 meridional variability influenced by both bathymetry and eddy activity (Kim and Orsi, 2014; Thompson et al.,
 173 2010). Fronts stabilize over major bathymetric features (e.g., the Pacific-Antarctic Ridge) but show maximum
 174 variability in flat basins. Due to eddy-mean flow interaction processes, frontal zones become greater downstream of
 175 topographic obstacles like the Campbell Plateau. Based on the observed frontal variability in the Pacific sector, the
 176 maximum total meridional frontal drift during 1993–2010 is approximately 80 km southward (at 150°E), and
 177 annual cycle amplitude is < 40 km (Kim and Orsi, 2014). To account for these frontal displacements, we first
 178 defined a baseline frontal zone as a ± 15 km strap in the normal direction from each climatological front. Then, to
 179 objectively identify eddy-front interactions, we applied a geometric criterion: an eddy was considered interacting
 180 when its boundary contacted the frontal zone. Since all analyzed eddies have a radius (R) > 30 km, this criterion
 181 effectively creates a dynamic interaction zone with a minimum half-width of 45 km (15 km + 30 km), which
 182 comfortably exceeds the observed ranges of frontal variability. To further ensure robustness, we conducted a
 183 sensitivity analysis by expanding the frontal zones to a ± 25 km strap (see Supplementary Materials), which
 184 confirmed that all key findings are insensitive to the exact zone definition.

185 The eddy-front interaction was then divided into three sequential phases: pre-cross-frontal, cross-frontal, and
 186 post-cross-frontal. CFEs were further categorized into four types: (1) Front-generated eddies, generated within the
 187 dynamic interaction zone and subsequently propagating away, (2) Front-dissipated eddies, propagating into the
 188 dynamic interaction zone and dissipated there, (3) Transient frontal eddies, both generated and dissipated within the
 189 same interaction zone, and (4) Complete CFEs, undergoing all three phases (pre-, cross-, and post-frontal) relative
 190 to the dynamic interaction zone. Both types (1) and (1) eddies were collectively classified as partial CFEs.
 191 Hereafter, all frontal zones refer to dynamic interaction zones. Notably, according to the definition, the partial
 192 frontal crossing eddies of Type 1 include rings pinched off from the meandering structures of a front.



193 **Figure 1. Study region. (a) Sea Level Anomaly (SLA) distribution on January 20th, 2022. (b) Spatial distribution of mean eddy**
 194 **kinetic energy (EKE) during 2000–2022. Thick colored lines from north to south represent the northern boundary of ACC**
 195 **(NB), the Subantarctic Front (SAF), the Polar Front (PF), the Southern Antarctic Circumpolar Current Front (SACCF) and**
 196 **the southern boundary of ACC (SB; Park et al., 2019). Significant seafloor topographies have been labeled, with UFZ denoting**
 197 **the Udintsev Fracture Zone. The abbreviation EFZ denotes the Eltanin Fracture Zone.**

198 **3 Results**

199 **3.1 Analysis of CFE characteristics**

200 CFE transport is active across all major ACC frontal zones in the Pacific sector (Figure 2). At each front,
 201 equatorward-moving CFEs consistently outnumber poleward-moving eddies (Figure 2b). CEs dominate
 202 equatorward CFEs, with CEs outnumbering AEs by a factor of ≥ 1.5 , while AEs prevail in poleward CFE motions.
 203 The resulting hierarchy of CFE prevalence is as follows: equatorward CEs are the most frequent (36% of total
 204 CFEs), followed by poleward AEs (30%) and equatorward AEs (18%), with poleward CEs (16%) being the least
 205 frequent. Among the different frontal zones, the SAF hosts the most eddy occurrences (30% of total CFEs),
 206 followed by the PF (27%), reflecting intense eddy-mean flow interactions around these two fronts. The
 207 northernmost NB (23% of total CFEs) and the SACCF (16%) exhibit comparable and moderate CFE levels, while
 208 the southernmost SB (7%) displays the lowest CFE exchanges.

209 The frontal system exhibits strong meandering patterns due to topographic steering, accompanied by spatially
 210 heterogeneous CFE distributions. CFE occurrence peaks downstream of prominent topographic features,
 211 particularly near the Campbell Plateau (150°E–180°E; 41% of total CFEs) and downstream of the Udintsev
 212 Fracture Zone (125°W–160°W; 38%), where multiple fronts converge (Figure 2a). Eddies may cross multiple
 213 fronts sequentially at these frontal convergent regions. The majority of eddies cross a single front (Figure 2c).
 214 Double-frontal crossings (total 411) occur preferentially at southern fronts (SACCF/SB; > 50% of cases; Figure 2d).
 215 Triple-frontal crossings are rare and primarily limited to the PF/SACCF/ SB system (Figure 2e), and no instances
 216 of quadruple-frontal crossings were observed.

217 Consistent with the ACC dynamics, over 70% of cross-frontal CEs and AEs propagate eastward (Figure 3), a
 218 notable contrast to the typical westward propagation of mesoscale eddies driven by Rossby waves in other ocean
 219 basins (Frenger et al., 2015). Short-distance movements ($< 2^\circ$) are more frequent for AEs at each front. In contrast,
 220 CEs dominate long-distance propagation, particularly at the SAF and PF. The majority of CEs propagate northward
 221 (over 64% of all CEs), while over 54% of AEs are oriented southward. The greater energetic content of CEs, as
 222 indicated by their dominance in long-distance transport, aligns with their role as primary agents of meridional
 223 exchange. These patterns highlight how ACC-steered eddy motions facilitate distinct transport pathways, with CEs
 224 disproportionately driving long-distance exchanges, particularly at major fronts such as the SAF and PF.

225 Most CFEs (99%) exhibit nonlinear characteristics (Figure 3k), confirming their capability to trap and advect
 226 water mass during their lifespan. In the nonlinearity regime ($\beta > 1$), equatorward-moving CEs constitute 72% of the
 227 total cross-frontal CEs, and 64% of the total cross-frontal AEs are poleward-moving ones (Figure 3k). In the high

228 nonlinearity regime ($\beta > 5$), the proportion of CEs is notably higher than AEs, consistent with the greater dynamic
 229 vigor of CEs observed in the above analyses. Therefore, the cross-frontal transport achieved by eddies, primarily
 230 equatorward-moving CEs and poleward-moving AEs, can facilitate the redistribution of distinct source water
 231 masses and reduce thermohaline gradients across frontal zones.

232 Cross-frontal CEs and AEs show similar distributions in lifespan, propagation distance, and size (Figure 4).
 233 Both types show a steep decline in abundance with increasing lifespan. Eddies with lifespans ≤ 50 days dominate,
 234 constituting 55% of the total eddy population, while only 3% exceed 200 days (Figure 4a). Propagation distances
 235 are confined predominantly to ≤ 400 km (56% of total CFEs). CEs slightly outnumber AEs at longer distances
 236 (400–1000 km; Figure 4b). Size distributions reveal that $\sim 75\%$ of the total sample have mean radii of 30–50 km
 237 (Figure 4c). Notably, CEs dominate at smaller radii (< 50 km), while AEs prevail among larger eddies. This
 238 distribution pattern is consistent with maximum radius statistics (Figure 4d). These CFE characteristics align with
 239 previously reported eddies in the Pacific sector (Duan et al., 2016).

240 Subsequently, we found distinct characteristics among types regarding their behaviors, when dividing the
 241 CFEs into partial CFEs, generated within and subsequently transported away (Type 1) and transported into and
 242 dissipated within the frontal zones (Type 2); transient CFEs, both generated and dissipated within the same frontal
 243 zone (Type 3); and complete CFEs, experiencing pre-crossing, crossing, and post-crossing phases (Type 4).
 244 Transient CFEs dominate numerically, accounting for 48% of all CFEs, and partially generated and dissipated
 245 CFEs constitute 23% and 20%, respectively (Figure 4a–d). These proportions collectively indicate that the frontal
 246 zones primarily act as terminal/starting areas for eddy life cycles, rather than a simple transit pathway. The
 247 proportion of transient CFEs falling within low-value parameter ranges is substantially higher than that of the other
 248 types: 59% of these eddies have lifespans ≤ 40 days and propagation distances ≤ 300 km, as well as 58% have
 249 mean radius ≤ 43 km and 63% have maximum radius ≤ 60 km. These values confirm the intrinsic nature of
 250 transient eddies as “generated and dissipated locally”, and reveal the constraining role of the frontal system on eddy
 251 evolution. In stark contrast, completely transported CFEs exhibit markedly different dynamical characteristics: 81%
 252 have lifespans > 40 days, 90% propagate > 300 km, and 68% have maximum radii > 60 km, indicating that these
 253 eddies have completely escaped the constraints of the local frontal environment and possess the capability for
 254 long-distance cross-frontal transport. Notably, among completely transported CFEs, small-scale CEs dominate
 255 significantly, with CEs accounting for 63%, while AEs account for only 37% for eddies with mean radii of 30–50
 256 km and maximum radii < 70 km. This polarity bias suggests that small-scale CEs may possess higher transport
 257 efficiency in cross-frontal material and energy exchange due to their unique dynamical structure.

258 Quantitative analysis of CFE types reveals distinct frontal-zone behaviors (Table 1). Transient eddies (Type 3)
 259 account for the largest proportion overall ($> 40\%$ by summing the transient AEs and CEs at each front), particularly
 260 at the two weaker southern fronts (SACCF and SB). Their proportions are lower at the SAF and PF, indicating that
 261 these two major fronts host more eddies that interact with areas outside the frontal zone during their lifecycle. For
 262 partially front-generated eddies (Type 1), both AEs and CEs exhibit relatively high proportions at the SAF and PF.
 263 At the southern SACCF and SB, however, the proportion of AEs drops markedly, whereas CEs show no such
 264 reduction. Among partially front-dissipated eddies (Type 2), the three northern fronts consistently show a higher
 265 proportion of CEs than AEs. At the two southern fronts, the pattern reverses, CE proportions decline sharply,
 266 causing a higher proportion of AEs. This suggests that in the southern fronts, local cross-frontal CEs are more
 267 readily generated and propagated outward, while being relatively resistant to dissipation.

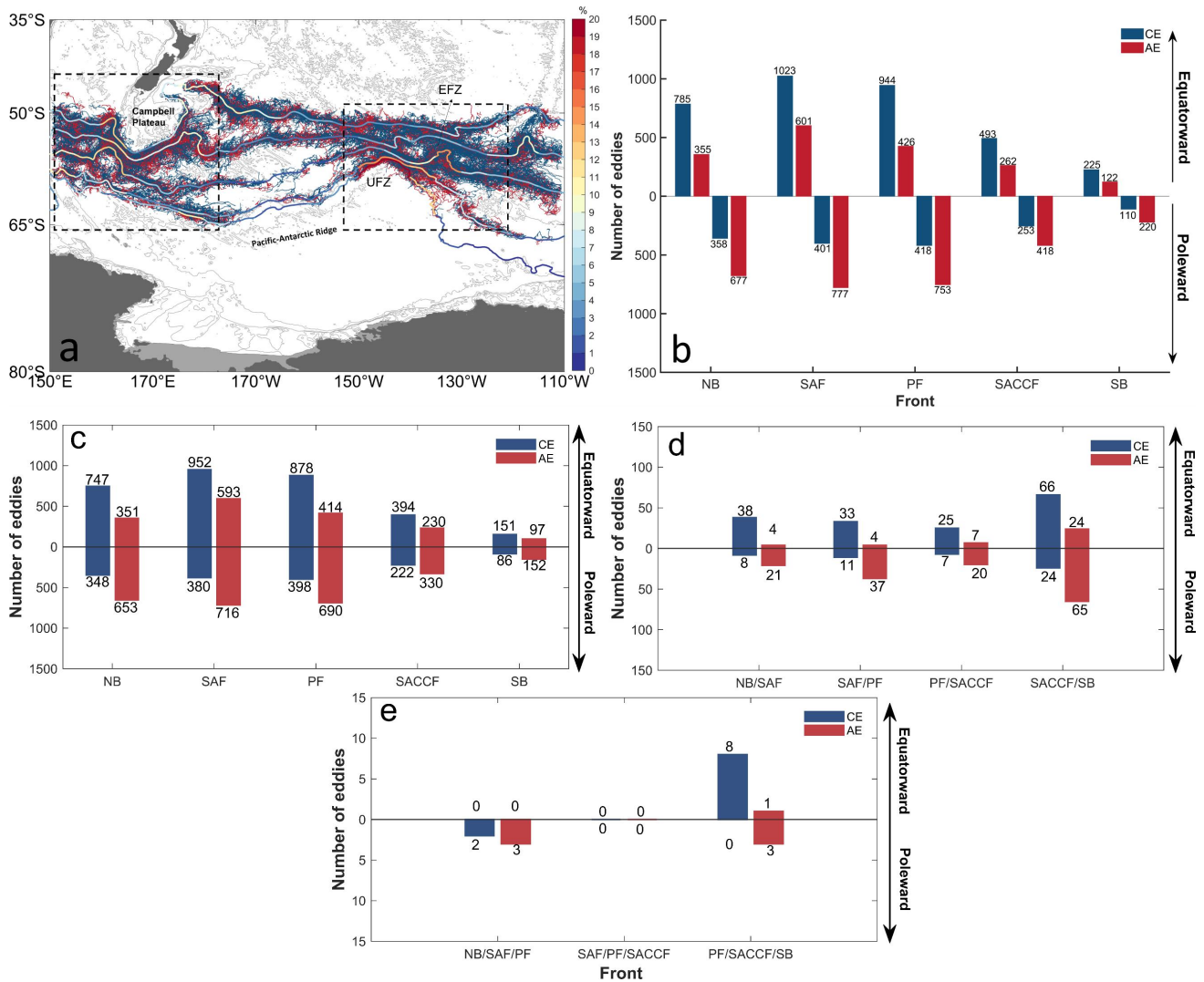
268 Regarding the partial CFEs, the proportion of front-generated AEs consistently exceeds that of front-dissipated
 269 AEs (except the SB), indicating that AEs are more likely to be generated within the fronts than to dissipate locally,
 270 particularly at the three northern fronts. For complete CFEs (Type 4), the proportion of AEs decreases with frontal
 271 latitude, while CEs reach their maximum proportions at the SAF and PF. These results demonstrate that different
 272 CFE types exhibit distinct behaviors when interacting with each front, shaped by frontal dynamics and latitudinal
 273 position.

274 Over the 22 years, the counts of poleward- and equatorward-moving eddies show pronounced interannual
 275 variability (Figure 4e). The annual abundance hierarchy, equatorward CEs $>$ poleward AEs $>$ equatorward AEs $>$
 276 poleward CEs, mirrors the total distribution in Figure 2b. In terms of EKE_T , CEs consistently exhibit approximately
 277 1.5-fold greater EKE_T than AEs (Figure 4f), consistent with their longer propagation distances and higher linearity
 278 (Figure 3). While the increasing trend in CEs' EKE_T is not statistically significant overall $(1.77 \pm 1.81) \times 10^6 \text{ m}^4 \text{ s}^{-2}$
 279 yr^{-1} ($p = 0.051$), this result is influenced by an anomalously low value in 2017, coinciding with an EKE minimum
 280 reported by Fu et al. (2023) in the central Pacific sector. Excluding this outlier yields a significant trend of $(2.27 \pm$
 281 $1.45) \times 10^6 \text{ m}^4 \text{ s}^{-2} \text{ yr}^{-1}$ ($p = 0.003$). In contrast, AEs' EKE_T displays a robust increase by $(2.27 \pm 0.94) \times 10^6 \text{ m}^4 \text{ s}^{-2}$
 282 yr^{-1} ($p < 0.001$). These results indicate that both eddy polarities contribute to the long-term EKE_T rise, with CEs
 283 exhibiting greater interannual variability. As established in Figure 2, equatorward-propagating CEs and
 284 poleward-propagating AEs dominate cross-frontal eddy abundance. Their EKE_T signals are substantially stronger
 285 than those of the overall CFE population, with significant increasing trends of $(2.43 \pm 2.45) \times 10^6 \text{ m}^4 \text{ s}^{-2} \text{ yr}^{-1}$ ($p =$
 286 0.045) for equatorward CEs and $(2.64 \pm 1.39) \times 10^6 \text{ m}^4 \text{ s}^{-2} \text{ yr}^{-1}$ ($p < 0.001$) for poleward AEs. Thus, beyond their

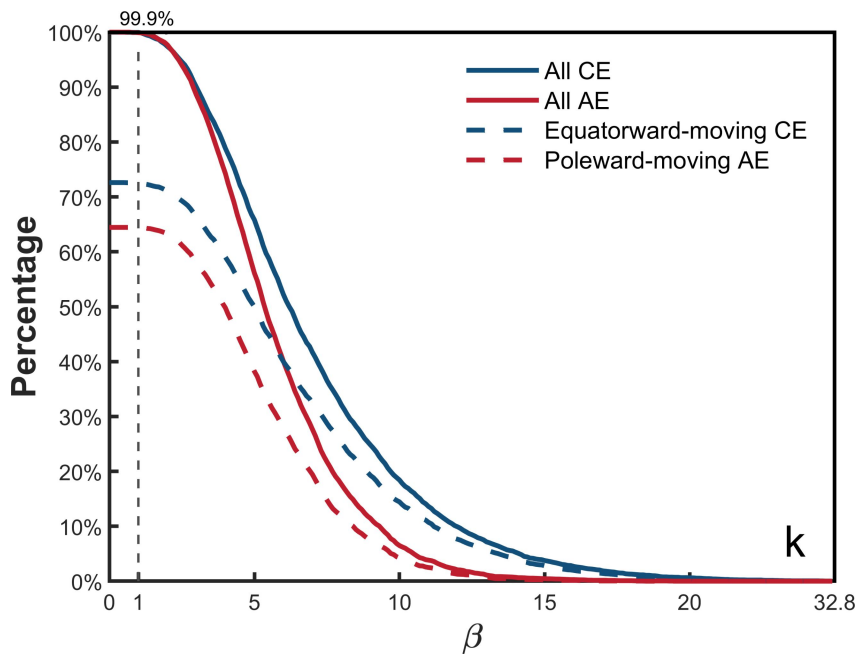
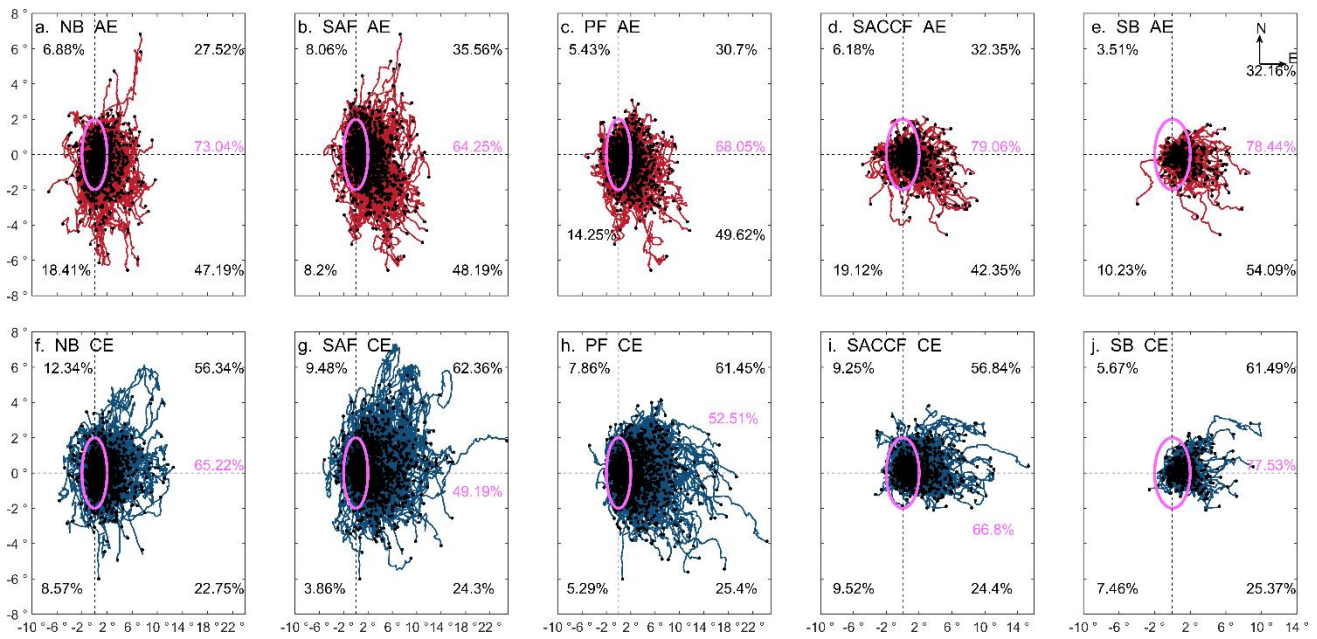
287 numerical dominance, these two subsets also govern the EKE level of CFEs and its intensification over the study
 288 period.

289 More specifically, all CFE types exhibit pronounced interannual variability and follow the same abundance
 290 hierarchy observed in Figure 4e in annual counts, with CEs dominating equatorward-moving eddies and AEs
 291 prevailing among poleward-moving ones (Figure 5a–d). Among the four types, complete CFEs of both polarities
 292 show the largest annual mean EKE_T , and display statistically significant increases over the study period with $(4.16$
 293 $\pm 3.54) \times 10^6 \text{ m}^4 \text{ s}^{-2} \text{ yr}^{-1}$ ($p = 0.024$) for CEs and $(3.17 \pm 2.49) \times 10^6 \text{ m}^4 \text{ s}^{-2} \text{ yr}^{-1}$ ($p = 0.015$) for AEs, respectively
 294 (Figure 5h). The dominant contributors to this enhancement are the same subsets that dominate abundance,
 295 equatorward-moving CEs and poleward-moving AEs, underscoring their role as the primary EKE_T source for
 296 complete CFEs. In contrast, partial and transient CFEs exhibit substantially lower EKE_T levels, with transient
 297 eddies showing the weakest energy content. Most of their increasing trends are not statistically significant (Figure
 298 5a–c), with the notable exception of transient AEs, which display a significant EKE_T increase (Figure 5c).

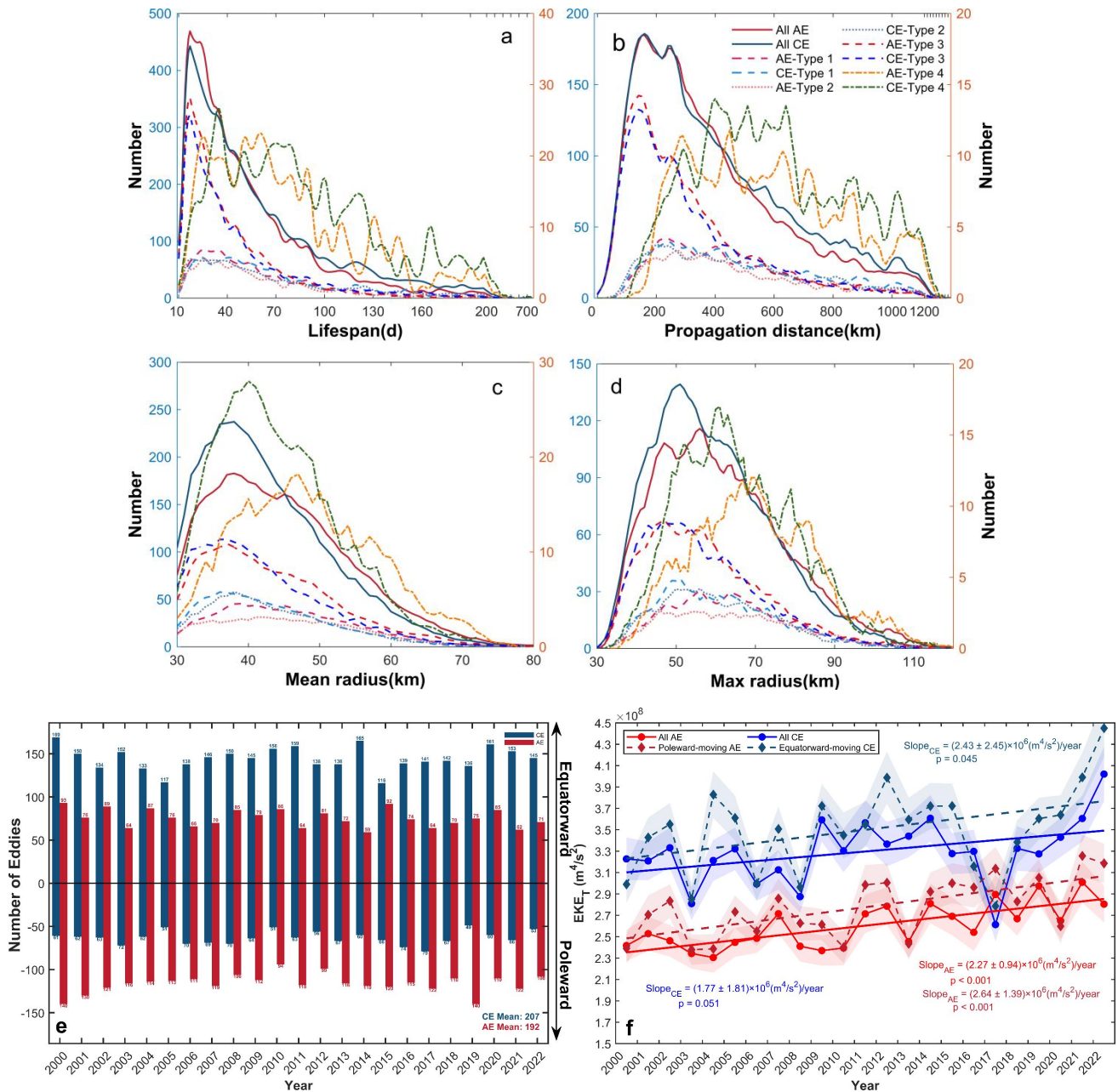
299 The relative contribution of each type to the total annual EKE_T reveals distinct energy compensation patterns
 300 between AEs and CEs (Figure 5i, j). For AEs, the primary energy compensation occurs between Type 1
 301 (front-generated) and Type 4 (complete frontal-crossing) eddies (correlation coefficient $R = -0.59$; $p = 0.003$),
 302 indicating that enhanced activity of partially frontal-generated AEs tends to suppress complete frontal-crossing AEs,
 303 and vice versa. A secondary compensation is between Type 2 and Type 3 ($R = -0.46$; $p = 0.027$). For CEs, the
 304 dominant compensation is between Type 3 (transient) and Type 4 (complete) eddies ($R = -0.66$; $p < 0.001$), with a
 305 modest compensation between Type 1 and Type 4 ($R = -0.44$; $p = 0.032$). These results suggest that more energetic
 306 complete CFEs tend to coexist with reduced activity of either partially frontal-generated or transient eddies. This
 307 compensatory relationship is critical for understanding mesoscale eddy-front interactions, particularly during the
 308 period of elevated EKE_T in complete CFEs.



309 **Figure 2. CFE trajectories and statistics of eddy counts. (a) CFE trajectories. The color along each front represents the relative**
 310 **occurrence of CFEs (%) per 5° latitudinal bin. The framed regions denote the area where active CFE activity occurs. (b) Total**
 311 **number of CFEs, divided into types of equatorward and poleward directions, shown as a function of the different ACC fronts;**
 312 **(c–e) Numbers of single-, double-, and triple-frontal crossing CFEs, respectively. Red represents anticyclonic eddies (AEs) and**
 313 **dark blue denotes cyclonic eddies (CEs).**



314 Figure 3. Relative movement trajectories of CFEs (a–j) and the percentage distribution of eddy nonlinearity β (k). In (a–j),
 315 black percentages represent the proportion of eddies moving in different quadrant directions calculated based on the end point
 316 of the trajectory, and purple percentages indicate the proportions of eddies with movement distances within a 2° range, with
 317 the coordinate origin (0°, 0°) denoting the eddies' generation locations. Note that eddies crossing multiple fronts may appear
 318 repeatedly at different frontal positions in this analysis.

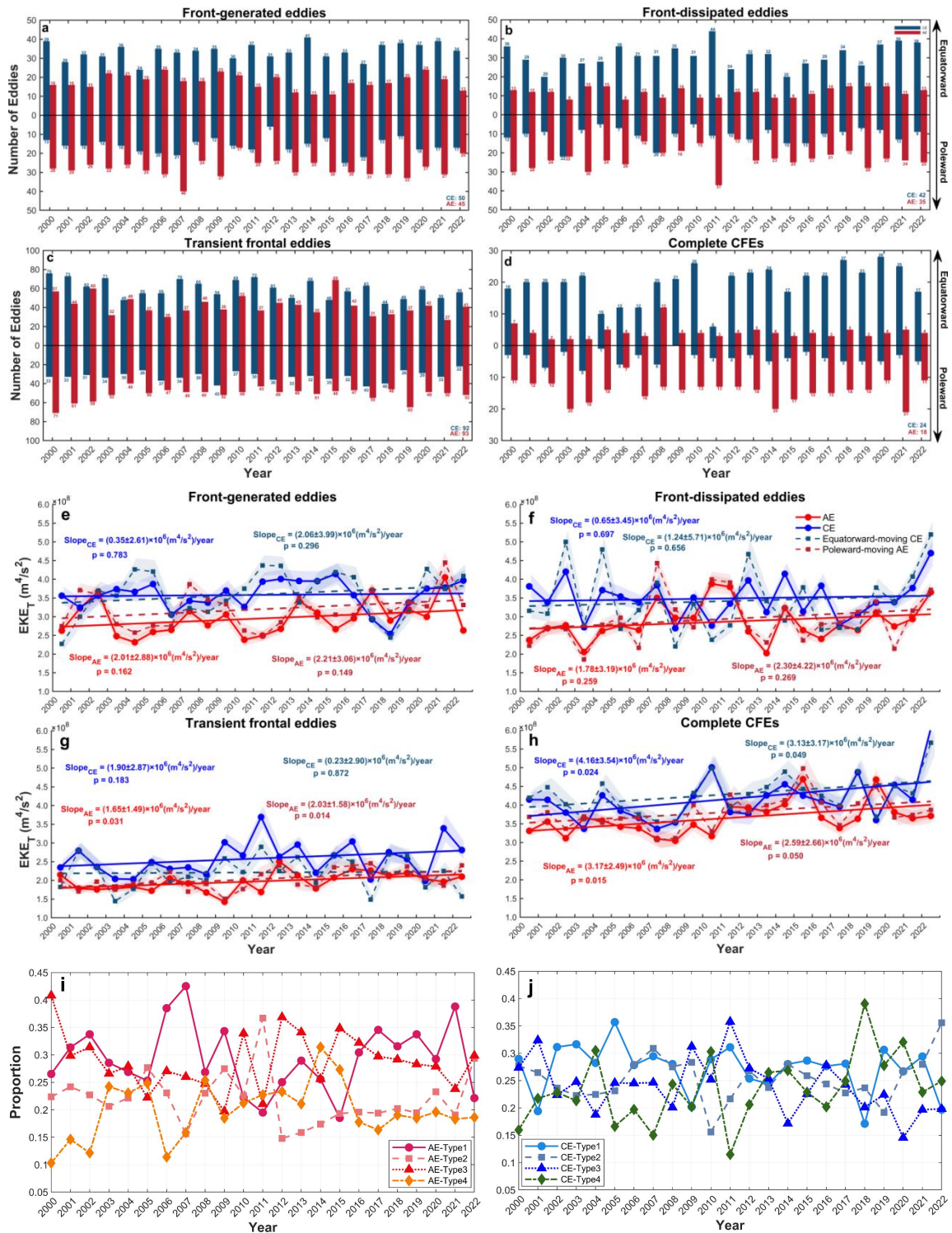


319 Figure 4. Statistical characteristics of different types of CFEs (a–d), time series of annual CFE counts (e), and annual mean
 320 EKE_T (f). Eddy counts according to (a) eddy lifespan, (b) propagation distance, (c) mean radius over lifespan, and (d)
 321 maximum radius in the lifespan. In (a–d), “All” represents all CFEs, “Type 1” denotes eddies front-generated and
 322 subsequently transported away, “Type 2” indicates eddies transported into the frontal zone and dissipated there, “Type 3”
 323 represents eddies generated and dissipated within the same frontal zone, and “Type 4” shows complete CFEs experiencing
 324 pre-crossing, crossing and post-crossing phases. The left Y-axis is for the first three subsets, and the right axis is for the Type 4
 325 eddies to clarify their distribution. The x-axes in (a) and (b) are compressed at higher values. In (e), all-year mean counts of
 326 CEs and AEs are indicated at the bottom right. In (f), the annual mean EKE_T for all AEs and CEs and the linear trends are
 327 depicted by dots, red and blue solid lines, respectively. The extracted subsets of poleward-moving AEs and
 328 equatorward-moving CEs are depicted by diamonds, red and blue dashed lines, respectively. Error shadings represent ± 1
 329 standard deviation, and slope values are given with $\pm 95\%$ confidence intervals.

330

Table 1. Proportions of numbers of different eddy types relative to the total number of CFEs at each frontal zone.

Type	Eddy polarity	NB	SAF	PF	SACCF	SB
(1) Front-generated eddies	AE	11.03%	12.21%	12.00%	8.84%	7.68%
	CE	10.11%	12.81%	12.59%	12.69%	10.49%
(2) Front-dissipated eddies	AE	8.41%	9.17%	9.21%	7.22%	9.45%
	CE	12.78%	11.74%	13.58%	6.52%	5.91%
(3) Transient frontal eddies	AE	22.71%	22.66%	20.43%	29.18%	31.17%
	CE	24.47%	18.49%	20.54%	30.37%	31.31%
(4) Complete CFEs	AE	5.29%	5.14%	4.76%	2.45%	2.22%
	CE	5.20%	7.78%	6.89%	2.73%	1.77%



331 Figure 5. Annual statistical characteristics of four types of CFEs, including their counts, mean EKE_T , and proportions of the
 332 summed EKE_T relative to all EKE_T . Time series of annual counts for (a) Front-generated eddies (Type 1), (b) Front-dissipated
 333 eddies (Type 2), (c) Transient frontal eddies (Type 3), and (d) Complete CFEs (Type 4). (e–h) Annual mean EKE_T for these
 334 four types of eddies. (i, j) Annual summed EKE_T for each type relative to all EKE_T for total CFEs. In (a–d), all-year mean
 335 counts of CEs and AEs are indicated at the bottom right. In (e–h), the annual mean EKE_T for all AEs and CEs and the linear
 336 trends are depicted by dots, red and blue solid lines, respectively. The extracted subsets of poleward-moving AEs and
 337 equatorward-moving CEs are depicted by diamonds, red and blue dashed lines, respectively. Error shadings represent ± 1
 338 standard deviation, and slope values are given with $\pm 95\%$ confidence intervals.

339 3.2 EKE_T evolution of complete CFEs during frontal crossing

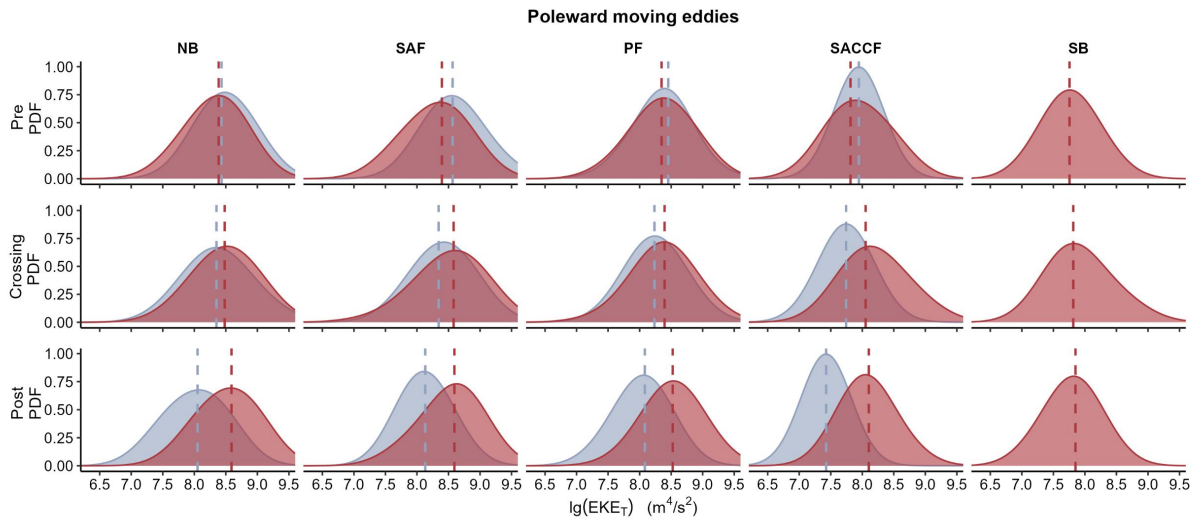
340 Although only a small fraction of eddies complete full cross-frontal transport (Table 1; Figure 5), these
 341 energetic features, originating in non-frontal zones and crossing entire frontal boundaries, likely dominate
 342 long-distance heat and material exchange between inter-frontal zones. Their rising EKE_T underscores their
 343 increasingly important dynamic role, motivating a closer examination of EKE_T evolution during frontal crossing.
 344 The Southern Hemisphere's intrinsic vorticity asymmetry (clockwise CEs vs. counterclockwise AEs) creates
 345 fundamental polarity differences in energy exchange when interacting with eastward frontal jets. Consequently,
 346 eddies of opposing polarities and directions are expected to exhibit distinct patterns of EKE_T variability during the
 347 cross-frontal transport.

348 Complete CFEs at the northern ACC fronts, NB, SAF, and PF, exhibit substantially higher EKE_T than those
 349 at the southern fronts (SACCF, SB; Figures 6, 7), consistent with their more frequent occurrence at the northern
 350 fronts (Table 1). For instance, mean EKE_T at the SAF ($4.21 \times 10^8 \text{ m}^4 \text{ s}^{-2}$) exceeds that at the SB ($9.51 \times 10^7 \text{ m}^4 \text{ s}^{-2}$)
 351 by $3.26 \times 10^8 \text{ m}^4 \text{ s}^{-2}$. During frontal crossing, EKE_T evolution exhibits clear polarity- and direction-dependence.
 352 Poleward-moving AEs consistently gain kinetic energy during crossing (3.23–88.02% increase), and experience
 353 further post-crossing amplification at the three northern fronts (43.52–71.76%), indicating sustained energy
 354 extraction from the mean flow (Figure 6; Table 2). In contrast, poleward CEs subsequently lose energy both during
 355 and after crossing, with reductions of 31.22–72.74% in the post-crossing phase. Equatorward-moving CFEs exhibit
 356 opposing behaviors (Figure 7; Table 2). AEs consistently lose energy, showing reductions of 2.59–27.47% during
 357 frontal crossing and further decline post-crossing (by 18.41–69.02%). In contrast, CEs generally gain energy, with
 358 post-crossing increases of 48.13–76.70% at the four northern fronts. This pattern reverses at the SB, where CEs
 359 show subsequent EKE_T loss (e.g., 43.02% decrease after crossing).

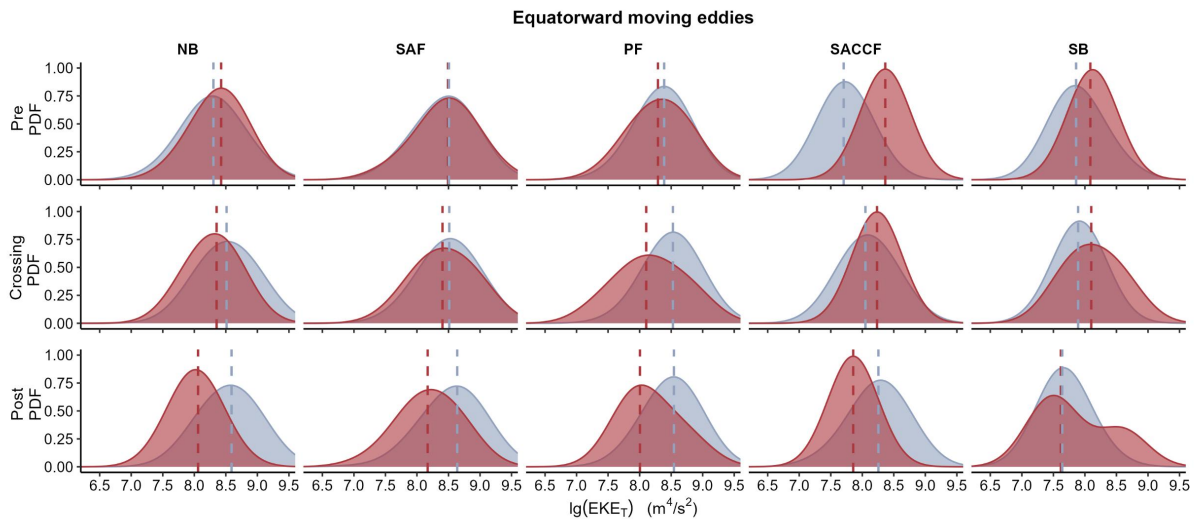
360 These results highlight fundamental asymmetries in eddy-front energy exchange governed by eddy polarity,
 361 movement direction, and frontal latitude. They also elucidate the energy compensation observed between
 362 frontal-generated partial/transient eddies and complete CFEs (as shown in Figure 5i, j): greater vorticity release to
 363 complete CFEs intrinsically reduces local eddy generation. Thus, the energy extraction from frontal jets fuels the
 364 complete frontal-crossing equatorward CEs and poleward AEs, contributing to their enhanced post-crossing
 365 energetics, consistent with the mesoscale principle of potential vorticity conservation. The anomalous energization
 366 of equatorward CEs at the SB, as well as lower pre-crossing EKE_T relative to in-crossing values for poleward AEs,
 367 is likely related to the weaker dynamical but stronger hydrographic characteristics of these southernmost fronts
 368 (Park et al., 2019; Thorpe et al., 2002; Vereshchaka et al., 2021).

369 **Table 2. Changes in mean EKE_T during different phases for complete cross-frontal eddies (CFEs) relative to pre-crossing**
 370 **values (+: increase; -: decrease). Crossing phases represent when eddies are in the frontal zones, while post-crossing phases**
 371 **indicate when eddies are moving away from the frontal zones. ‘-’ denotes no data.**

Direction	Eddy polarity	Phase	NB	SAF	PF	SACCF	SB
poleward-moving	AE	crossing	+51.80%	+61.92%	+3.23%	+88.02%	+67.03%
		post	+71.76%	+69.88%	+43.52%	+21.43%	+3.44%
	CE	crossing	-8.44%	-44.63%	-32.58%	-37.68%	-
		post	-31.22%	-72.74%	-57.63%	-69.77%	-
equatorward-moving	AE	crossing	-18.51%	-2.59%	-7.91%	-27.47%	-3.26%
		post	-58.00%	-46.10%	-18.41%	-69.02%	-27.91%
	CE	crossing	+64.28%	+17.91%	+47.86%	+54.70%	-10.89%
		post	+75.78%	+52.33%	+48.13%	+76.70%	-43.02%



372 **Figure 6. Probability density function (PDF) of EKE_T for poleward-moving CFEs in pre-crossing, crossing, and post-crossing**
 373 **phases. Dashed lines indicate median EKE_T values. Blue and red colors represent CEs and AEs, respectively.**



374 **Figure 7. Probability density function (PDF) of EKE_T for equatorward-moving CFEs in pre-crossing, crossing, and**
 375 **post-crossing phases. Dashed lines indicate median EKE_T values. Blue and red colors represent CEs and AEs, respectively.**

376 **3.3 Thermohaline transport effects of CFEs**

377 Argo θ - S profiles (Figure 8) reveal that cyclonic eddies (CEs) and anticyclonic eddies (AEs) exhibit distinct,
 378 polarity-dependent hydrographic signatures within the same interfrontal zones. CEs consistently contain colder,
 379 fresher water with shallower isopycnals (upper 1000 dbar), whereas AEs are characterized by warmer, saltier water
 380 and deeper isopycnals. These contrasts underscore the role of nonlinear eddies in mediating cross-frontal exchange.
 381 However, a subset of AEs in the SACCF-PF zone trap anomalously cold, fresh polar waters ($\theta_{min} = -1.76^{\circ}\text{C}$ and S
 382 < 34.0 psu), similar to those observed in some AEs within the SB-SACCF zone, indicating that AEs can also
 383 transport polar waters equatorward. Notably, eddy-induced vertical motions, upwelling in CEs and downwelling in
 384 AEs, produce vertical displacements but do not alter θ - S properties of source water columns (Falkowski et al., 1991;
 385 Li et al., 2022). Therefore, this mechanism can only account for overlapping θ - S signatures that arise from vertical
 386 repositioning of the same water mass, rather than true cross-frontal modification.

387 Analysis of radius-normalized θ - S distributions reveals distinct water mass signatures in CEs and AEs across
 388 northern interfrontal zones (SAF-NB, PF-SAF, and SACCF-PF). Core water masses, especially Subantarctic Mode
 389 Water (SAMW) and Antarctic Intermediate Water (AAIW), are not circumpolarly uniform but exhibit substantial
 390 regional variability (Bostock et al., 2013; Li et al., 2022). For instance, within the Pacific sector, the salinity
 391 minimum of AAIW ranges from ~ 34.2 in the southeast Pacific formation region to greater than 34.5 in the Tasman
 392 Sea after mixing (Bostock et al., 2013). Similarly, SAMW exhibits distinct spatial patterns in its formation and
 393 properties (Li et al., 2021). Accordingly, the ranges in Table 3 are intended as a practical guide for identifying
 394 water masses within the specific Pacific sectoral context of this study.

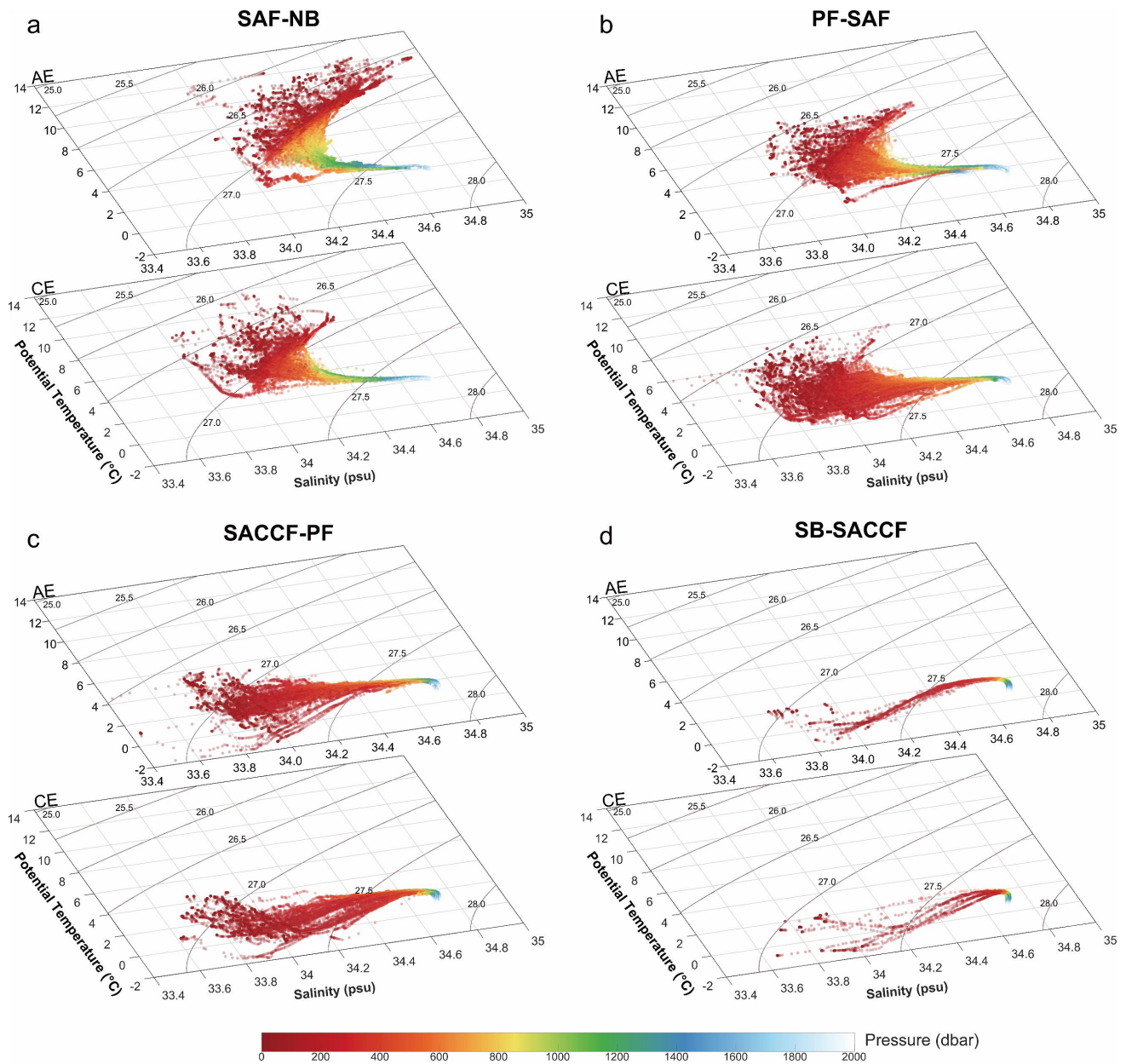
395 Between the SAF and NB, well-defined layers of SAMW, AAIW, and Upper Circumpolar Deep Water
 396 (UCDW) are observed from the upper to lower layer in the AE (Figure 9d, j), confirming their local origin within
 397 the Antarctic Convergence Zone. Conversely, the CE in the same zone shows markedly different θ - S structure
 398 (Figure 9a, g), with upper layers (< 1000 dbar) lacking SAMW/AAIW signatures and instead containing colder,
 399 fresher waters of southern origin. Neutral density (γ^n) surfaces in the CE are approximately 200 dbar shallower than
 400 in the AE, demonstrating that CEs effectively transport high-potential-energy southern waters into the SAF-NB
 401 zone. This establishes strong mesoscale potential energy contrasts between the low-potential-energy waters in AEs
 402 and the high-potential-energy waters in CEs, an energetic precondition for baroclinic instability via the release of
 403 available potential energy (Fu et al., 2023).

404 In the PF-SAF region, both the CE and AE maintain thermohaline contrasts similar to those in the SAF-NB
 405 zone but with reduced magnitude, preserving the characteristic warmer/saltier AE and colder/fresher CE signatures

406 (the middle panels of Figure 9). Notably, only the CE's upper layer exhibits distinct Winter Water (WW)
407 characteristics, confirming their southern origins. Below this, the normalized CE sequentially displays UCDW and
408 LCDW, while the AE shows only UCDW beneath the relatively warm and salty Antarctic Surface Water within the
409 upper 2000 dbar. The vertical isopycnal structure reveals depth-dependent displacements: in the near-surface layer,
410 the CE's isopycnal $\gamma^\sigma=27.1 \text{ kg/m}^3$ is ~ 100 dbar shallower than the AE, while at intermediate depths, the CE's
411 isopycnal $\gamma^\sigma=27.6 \text{ kg/m}^3$ (400–600 dbar) is ~ 500 dbar shallower than the AE (~ 1000 dbar).

412 The thermohaline anomalies between CE and AE still exist in the SACCF-PF zone (the right panels of Figure
413 9). In the CE, a subsurface WW layer overlies a warm UCDW core, with LCDW dominating below 1000 dbar,
414 showing a characteristic of waters south of the SACCF (Aoki et al., 2013; Auger et al., 2021). While the AE also
415 contains these water masses, they show weaker WW expression, a more pronounced θ_{\max} core, and vertically
416 extended UCDW, reflecting their relatively northern origins. Isopycnals in the CE remain consistently 300–400
417 dbar shallower than in the AE throughout the water column.

418 Therefore, the normalized AE and CE possess distinct water mass distributions within the same inter-frontal
419 zones, marked by profound isopycnal thermohaline differences. AEs and CEs transport their respective source
420 water masses into the same zones, amplifying mesoscale hydrographic variability. The above comparative analysis
421 demonstrates that cross-frontal CEs play a dominant role in meridional water mass transport, particularly in the
422 SAF-NB and SACCF-PF zones, consistent with their greater dynamical vigor. This cross-frontal exchange reduces
423 baroclinicity between interfrontal zones while enhancing mesoscale available potential energy within individual
424 zones.

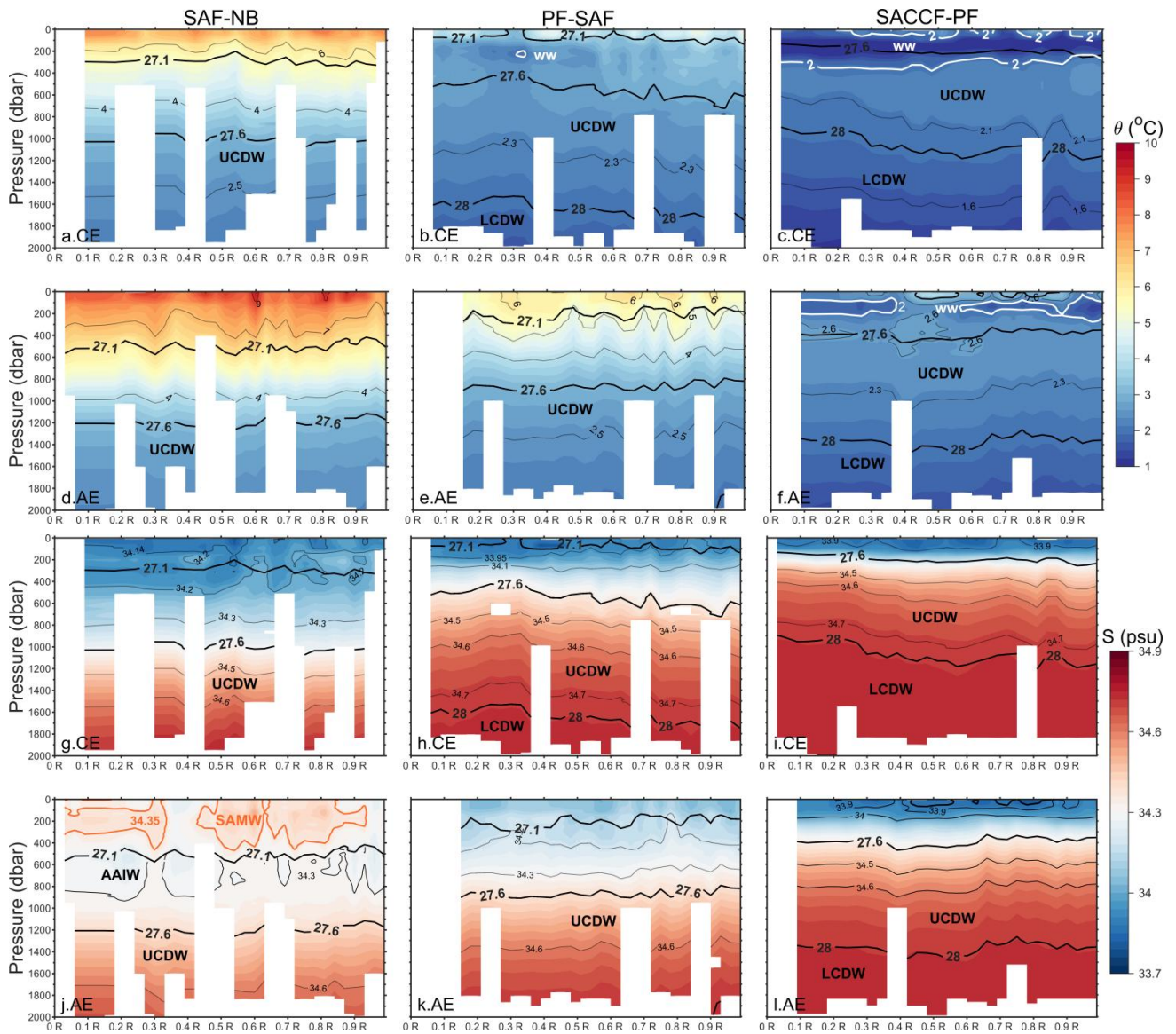


425 **Figure 8. Potential temperature-salinity (θ -S) diagrams in the eddy interiors observed in different inter-frontal zones. (a)**
 426 **SAF-NB; (b) PF-SAF; (c) SACCF-PF; (d) SB-SACCF.**

427 **Table 3. Criteria for the division of water masses according to potential temperature (θ , °C), salinity (S , psu) and neutral**
 428 **density (γ^n , kg/m³). Note: The ranges listed, particularly for SAMW and AAIW, are primarily representative of the Pacific**
 429 **sector of the Southern Ocean.**

Water mass	θ (°C)	S (psu)	γ^n (kg/m³)	Reference
SAMW		34.35–34.60	27.00–27.20	Carter et al., 2022; Bostock et al., 2013; Herraiz-Borreguero and Rintoul, 2011
AAIW		S_{\min} 34.28–34.40	27.10–27.60	Bostock et al., 2013; Xia et al., 2022; Valla et al., 2018
UCDW	θ_{\max}		27.55–28.00	Naveira Garabato et al., 2002
LCDW		S_{\max}	28.00–28.27	
WW	θ_{\min} < 2.00			

430 *SAMW, Subantarctic Mode Water; AAIW, Antarctic Intermediate Water; UCDW, Upper Circumpolar Deep Water; LCDW, Lower
 431 Circumpolar Deep Water; WW, Winter Water.



432 **Figure 9.** Sectional distributions of θ (a–f) and S (g–l) along normalized eddy radius (R) direction in the interfrontal zones of
 433 SAF-NB (the left panels), PF-SAF (the middle panels), and SACCF-PF (the right panels). Black thick contours indicate neutral
 434 density (σ_n , kg/m^3), thin contours represent θ or S isolines, respectively.

435 **4 Discussion**

436 This study reveals a fundamental polarity- and direction-dependent asymmetry in cross-frontal eddy (CFE)
 437 dynamics within the Pacific sector of the SO. This asymmetry manifests in three key aspects: (1) a distinct
 438 abundance hierarchy among CFE types, (2) contrasting *EKE* intensities and trends, and (3) polarity- and
 439 direction-selective energy transfers during eddy-frontal jet interactions. The observed hierarchy, in which CEs
 440 predominantly migrate equatorward and AEs poleward, aligns with established eddy dynamics in the SO (He et al.,
 441 2023; Li et al., 2022; Patel et al., 2019). Beyond abundance, the dominant types (equatorward CEs and poleward
 442 AEs) exhibit superior energetic characteristics, including higher *EKE* levels (Figure 4f), longer propagation
 443 distances (Figure 3), and stronger nonlinearity compared to their counterparts. Our results demonstrate that
 444 substantial energy gain during frontal crossing sustains the enhanced energetics of these two dominant complete
 445 CFE types, as illustrated in Figure 11. Moreover, the energy compensation relationships (Figure 5i, j) suggest that
 446 partial and transient CFEs of the same dominant polarity-direction combinations likely follow a similar
 447 energization mechanism. Taken together, these findings indicate that polarity- and direction-dependent eddy-front
 448 interactions fundamentally govern CFE energetics and, consequently, their capacity to drive meridional heat and
 449 material transport across Southern Ocean frontal zones.

450 Although CFE abundance shows no significant trend over 2000–2022, both polarity groups experienced
 451 substantial EKE_T intensification, with CEs gaining energy at $(2.27 \pm 1.45) \times 10^6 \text{ m}^4 \text{ s}^{-2} \text{ yr}^{-1}$ (excluding the
 452 anomalously low 2017 value) and AEs at $(2.27 \pm 0.94) \times 10^6 \text{ m}^4 \text{ s}^{-2} \text{ yr}^{-1}$. The increasing trends are also robust in
 453 terms of annual area-weighted mean *EKE* ($EKE = EKE_T/S$, where *S* is the total area of an eddy; Figure S1 in the
 454 Supplementary Materials), with trends of $3.71 \pm 2.08 \text{ cm}^2 \text{ s}^{-2} \text{ yr}^{-1}$ for CEs and $2.58 \pm 0.97 \text{ cm}^2 \text{ s}^{-2} \text{ yr}^{-1}$ for AEs. The
 455 *EKE* enhancements are even more pronounced for the dominant subsets, equatorward CEs and poleward AEs
 456 (Figures 4, S1). These rates substantially exceed previously reported *EKE* trends. Hogg et al. (2015) estimated a
 457 regional mean *EKE* increase of $14.9 \pm 4.1 \text{ cm}^2 \text{ s}^{-2} \text{ decade}^{-1}$ under intensifying westerlies in the Pacific sector
 458 (1990–2015). Similarly, Zhang et al. (2021) documented an *EKE* increase of $< 20 \text{ cm}^2 \text{ s}^{-2} \text{ decade}^{-1}$ south of New
 459 Zealand and downstream of the Campbell Plateau, identified as the only region with significant *EKE* rise in the SO
 460 during 1993–2018. The *EKE* trends for CFEs presented here are considerably larger than these basin-scale
 461 estimates. In contrast, non-CFEs exhibit lower *EKE* levels and no comparable EKE_T increase (Figure 10). The
 462 significant area-weighted mean *EKE* trend for non-frontal crossing CEs is also weaker (Figure S2). These contrasts
 463 suggest that the overall *EKE* increase in the Pacific sector is primarily attributable to CFEs. Non-CFEs contribute
 464 little to, or may even obscure, the observed *EKE* trends. This finding implies that eddy-front interactions, rather

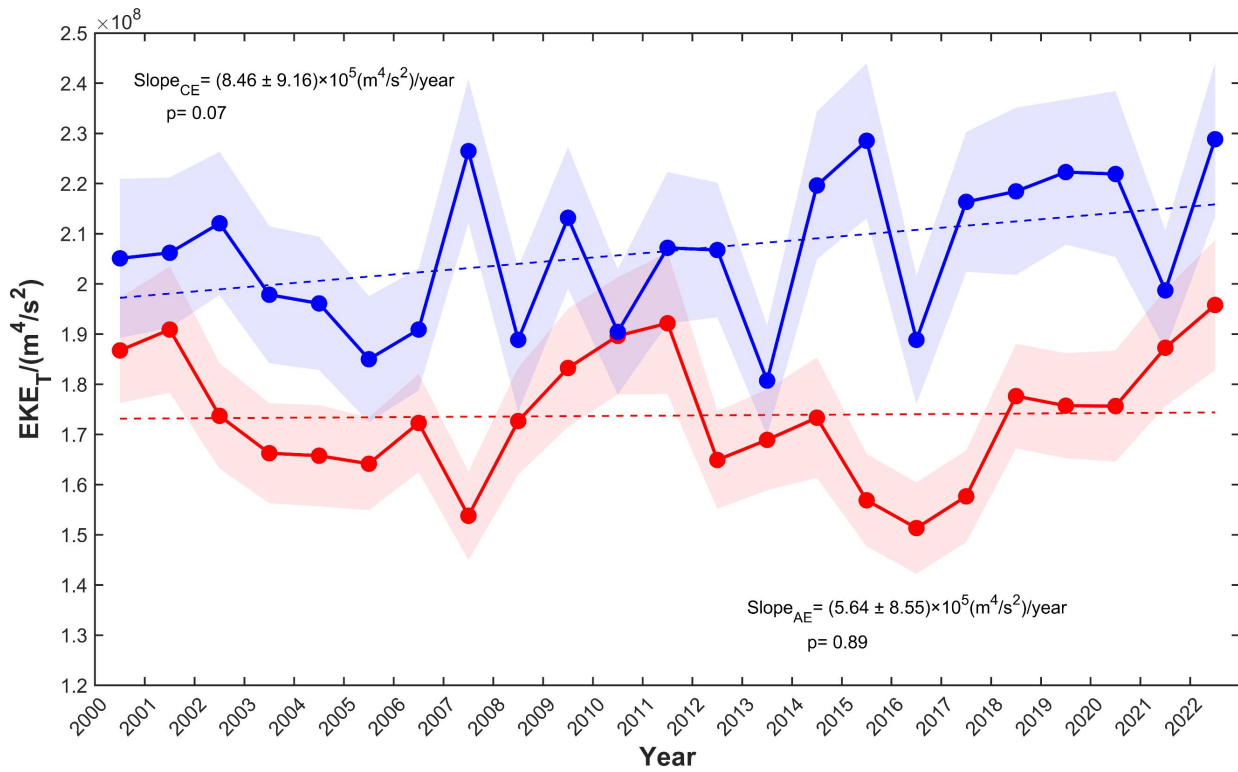
465 than basin-scale wind forcing alone, may be the primary driver of recent *EKE* trends in the Pacific sector of the SO.

466 Our results suggest that the enhanced wind stress (Hogg et al., 2015; Menna et al., 2020) could preferentially
467 energize cross-frontal activity, especially the CFEs achieving complete frontal crossing (Figure 5). The
468 predominance of equatorward CEs aligns with intensified Ekman transport patterns reported by Shi et al. (2025),
469 also suggesting wind-driven facilitation of meridional eddy migration. Building on Fu et al.'s (2023) framework of
470 wind-driven energy pathways (baroclinic: mean kinetic energy \rightarrow mean available potential energy \rightarrow mesoscale
471 available potential energy \rightarrow EKE; barotropic: mean kinetic energy \rightarrow EKE), we found that only equatorward CEs
472 and poleward AEs gain kinetic energy from frontal jets (Table 2; Figures 6, 7). This energization likely arises from
473 two synergistic mechanisms: (1) barotropic instability from enhanced horizontal shear when eddy rotation aligns
474 with the eastward jet (Qiu et al., 2024), and (2) baroclinic instability triggered by potential energy release for
475 enhanced hydrographic gradients with ambient waters (Fu et al., 2023). Conversely, significant energy losses of
476 poleward CEs and equatorward AEs during frontal crossing, possibly due to counter-rotational turbulent dissipation
477 (Dong et al., 2017; Jan et al., 2017) and upwelling (downwelling)-induced baroclinicity reduction with the ambient
478 waters.

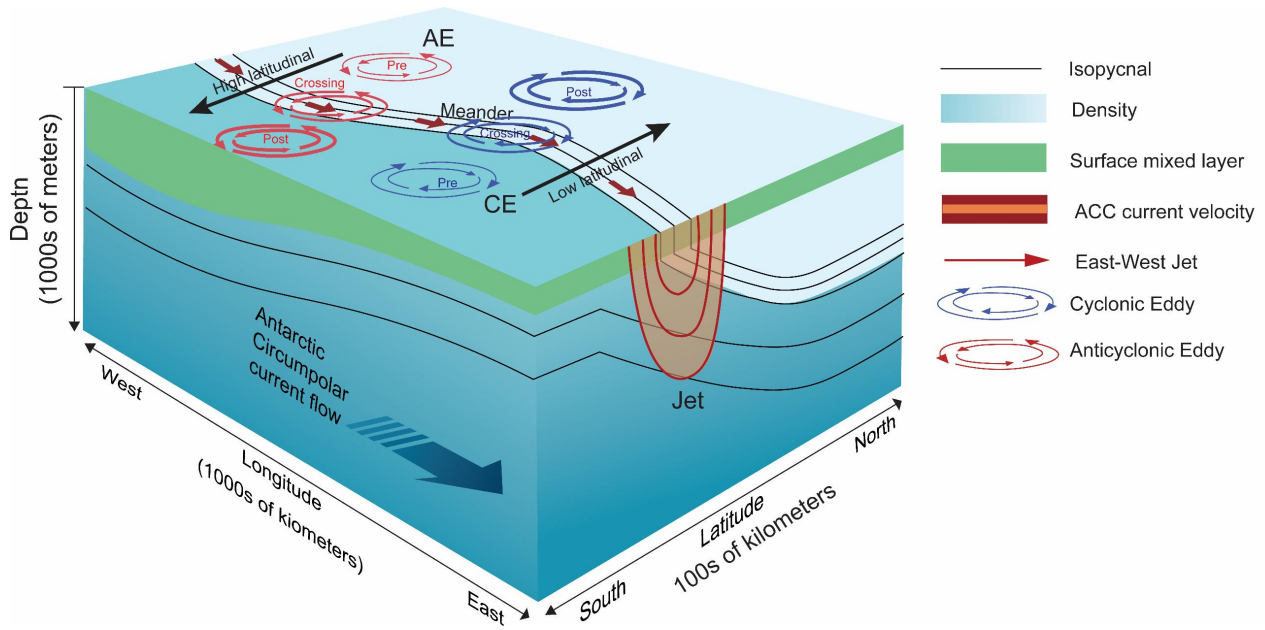
479 Intensifying and poleward-shifting westerlies have emerged as a dominant dynamic forcing mechanism in the
480 SO (Behrens and Bostock, 2023; Hogg et al., 2015). Meanwhile, buoyancy forcing from meridionally
481 inhomogeneous ocean warming has been shown to accelerate the ACC at 48°S–58°S (Shi et al., 2021). Our
482 results demonstrate that CFEs play a vital role in mediating the oceanic response to these forcings by compensating
483 for heat transport (Figure 9). By facilitating equatorward cold-water transport via CEs and poleward warm-water
484 transport via AEs, CFEs reduce cross-frontal water mass property gradients. This process effectively buffers wind-
485 or warming-induced increases in baroclinicity, thereby maintaining the SO's thermal equilibrium and modulating
486 the ACC's response to external forcing. These findings highlight the dual role of CFEs as both energy transporters
487 and dynamical stabilizers in a changing climate.

488 This study has several limitations that should be noted. First, the analysis does not account for potential
489 interannual or seasonal variations in frontal positions. However, a comprehensive sensitivity analysis, in which the
490 frontal zone half-width was expanded to $\pm(25+R)$ km, confirms that all key conclusions remain qualitatively and
491 statistically robust (see Supplementary Materials, Tables S1 and S2, and Figures S3–S6). Second, the hydrographic
492 analysis utilized all qualified Argo profiles from 2000 to 2022 without segregating interannual or seasonal
493 variability, which may introduce some uncertainty into the normalized water mass properties. Finally, while this
494 study focuses on eddy characteristics, it does not evaluate the dynamic properties of the frontal jets themselves. A

495 detailed analysis of jet variability and energy transfer is essential for a more comprehensive mechanistic
 496 understanding of eddy-jet interactions and represents an important direction for future research.



497 **Figure 10.** Time series of annual mean EKE_T for eddies in the interfrontal zones. EKE_T is shown by blue solid line for CEs and
 498 red solid line for AEs, with linear regression indicated by dashed lines, error shadings representing one standard deviation,
 499 and slope values given with $\pm 95\%$ confidence intervals.



500 Figure 11. Illustrations of EKE variations during frontal crossing for poleward AEs and equatorward CEs (modified from
 501 Figure 1 in Chapman et al., 2020). The thickness of rotational velocity vectors represents relative flow intensity.

502 **5 Conclusions**

503 This study provides a comprehensive characterization of cross-frontal eddies (CFEs) in the Pacific sector of
504 the Southern Ocean, revealing fundamental asymmetries that govern their role in meridional transport and energy
505 exchange. Through the integration of multi-decadal satellite altimetry and in-situ hydrographic data, we have
506 demonstrated that CFE activity is not random but follows a well-defined polarity- and
507 direction-dependent hierarchy. The predominance of equatorward-moving cyclonic eddies
508 (CEs) and poleward-moving anticyclonic eddies (AEs) reflects an intrinsic organization in cross-frontal exchange
509 pathways that has profound implications for Southern Ocean dynamics.

510 Three key findings emerge from our analysis. First, the observed CFE abundance hierarchy is complemented
511 by significant differences in energetic characteristics, with the dominant types (equatorward CEs and poleward AEs)
512 exhibiting superior kinetic energy levels, longer propagation distances, and stronger nonlinearity. Second, these
513 eddies experience sustained energization through polarity-selective energy transfers during frontal crossings,
514 gaining kinetic energy from the eastward frontal jets while their counterparts experience energy dissipation. The
515 intensification of CFE activity has occurred over the past two decades, with *EKE* trends substantially exceeding
516 previous basin-scale estimates, suggesting that eddy-front interactions, rather than wind forcing alone, drive recent
517 energetic changes in the region. Third, hydrographic analyses confirm that CFEs function as effective transporters
518 of distinct water masses, with CEs and AEs maintaining sharp thermohaline contrasts within the same interfrontal
519 zones. This cross-frontal exchange reduces large-scale baroclinicity while enhancing mesoscale available potential
520 energy, creating a dynamic balance that regulates meridional heat transport.

521 As climate change intensifies westerly winds and modifies buoyancy forcing, CFEs are likely to play an
522 increasingly important role in modulating the ACC's response to external forcing. Their ability to maintain thermal
523 equilibrium across frontal zones highlights their significance for understanding future changes in Southern Ocean
524 circulation, carbon uptake, and global climate feedbacks. Future research should focus on quantifying the precise
525 contribution of CFEs to meridional heat and carbon fluxes and investigating how their stabilizing role might evolve
526 under continued climate change.

527 **Data availability**

528 The satellite altimeter data are available online at the Copernicus Marine Service (the CMEMS all-satellite L4
529 SLA product at <https://doi.org/10.48670/moi-00148>). The data were accessed and downloaded on 18th December,
530 2025. The frontal data used in this study were sourced from Park et al. (2019) at <https://doi.org/10.17882/59800>.
531 Argo profiles are available at the website of <https://argo.ucsd.edu/data/>.

532 **Author contributions**

533 Huimin Wang: Methodology, Software, Formal analysis, Investigation, Data curation, Writing-original draft,
534 Visualization. Lingqiao Cheng: Conceptualization, Methodology, Resources, Writing-original draft,
535 Writing-review & editing, Supervision, Project administration, Funding acquisition. Erik Behrens: Validation,
536 Writing-review & editing. Zhuang Chen: Validation, Writing-review & editing. Jennifer Devine: Writing-review &
537 editing. Guoping Zhu: Resources, Writing-review & editing, Funding acquisition.

538 **Competing Interests**

539 The authors declare that they have no conflict of interest.

540 **Acknowledgments**

541 We thank the Key Laboratory of Sustainable Exploitation of Oceanic Fisheries Resources, Shanghai Ocean
542 University and the Joint Research Center on Antarctic Marine Science supported by Shanghai Ocean University,
543 Earth Sciences New Zealand, and the University of Otago for their support and the utilization of their laboratory
544 facilities.

545 **Financial support**

546 This work was funded by the National Key Research and Development Program of China (grant no.
547 2023YFE0104500), the National Natural Science Foundation of China (grant no. 42130402), Shanghai Top-tier
548 Talent Program of Eastern Talent Plan (grant no. BJKJ2024059), and supported by the Catalyst Fund from
549 Government funding, administered by the Royal Society Te Apārangi.

550 **References**

- 551 Aoki, S., Kitade, Y., Shimada, K., Ohshima, K. I., Tamura, T., Bajish, C. C., Moteki, M., and Rintoul, S. R.: Widespread
 552 freshening in the Seasonal Ice Zone near 140°E off the Adélie Land Coast, Antarctica, from 1994 to 2012. *J.*
 553 *Geophys. Res. Oceans.*, 118(11), 6046–6063, <https://doi.org/10.1002/2013JC009009>, 2013.
- 554 Auger, M., Morrow, R., Kestenare, E., Sallée, J.-B., and Cowley, R.: Southern Ocean in-situ temperature trends over 25
 555 years emerge from interannual variability. *Nat. Commun.*, 12(1), 1840,
 556 <https://doi.org/10.1038/s41467-020-20781-1>, 2021.
- 557 Barthel, A., McC. Hogg, A., Waterman, S., and Keating, S.: Jet–Topography Interactions Affect Energy Pathways to the
 558 Deep Southern Ocean. *J. Phys. Oceanogr.*, 47(7), 1799–1816, <https://doi.org/10.1175/JPO-D-16-0220.1>, 2017.
- 559 Behrens, E., and Bostock, H.: The Response of the Subtropical Front to Changes in the Southern Hemisphere Westerly
 560 Winds—Evidence From Models and Observations. *J. Geophys. Res. Oceans.*, 128(2), e2022JC019139,
 561 <https://doi.org/10.1029/2022JC019139>, 2023.
- 562 Belkin, I. M., and Gordon, A. L.: Southern Ocean fronts from the Greenwich meridian to Tasmania, *J. Geophys. Res.*,
 563 101, 3675–3696, <https://doi.org/10.1029/95JC02750>, 1996.
- 564 Bostock, H. C., Sutton, P. J., Williams, M. J., and Opdyke, B. N.: Reviewing the circulation and mixing of Antarctic
 565 Intermediate Water in the South Pacific using evidence from geochemical tracers and Argo float trajectories,
 566 *Deep Sea Research Part I: Oceanographic Research Papers*, 73, 84–98, doi:10.1016/j.dsr.2012.11.007, 2013.
- 567 Carter, L., Bostock-Lyman, H., and Bowen, M.: Water masses, circulation and change in the modern Southern Ocean, in:
 568 *Antarctic Climate Evolution (Second Edition)*, edited by: Florindo, F., Siebert, M., De Santis, L., and Naish, T.,
 569 Elsevier, Amsterdam, 165–197, <https://doi.org/10.1016/B978-0-12-819109-5.00003-7>, 2022.
- 570 Chapman, C., and Sallée, J.-B.: Isopycnal Mixing Suppression by the Antarctic Circumpolar Current and the Southern
 571 Ocean Meridional Overturning Circulation. *J. Phys. Oceanogr.*, 47(8), 2023–2045,
 572 <https://doi.org/10.1175/JPO-D-16-0263.1>, 2017.
- 573 Chapman, C. C., Lea, M.-A., Meyer, A., Sallée, J.-B., and Hindell, M.: Defining Southern Ocean fronts and their
 574 influence on biological and physical processes in a changing climate, *Nat. Clim. Change.*, 10(3), 209–219,
 575 <https://doi.org/10.1038/s41558-020-0705-4>, 2020.
- 576 Chelton, D. B., Schlax, M. G., and Samelson, R. M.: Global observations of nonlinear mesoscale eddies, *Prog. Oceanogr.*,
 577 91(2), 167–216, <https://doi.org/10.1016/j.pocan.2011.01.002>, 2011.
- 578 Copernicus Marine Service: Global Ocean Gridded L4 Sea Surface Heights And Derived Variables Reprocessed 1993
 579 Ongoing (SEALEVEL_GLO_PHY_L4_MY_008_047), Mercator Ocean International [data
 580 set], <https://doi.org/10.48670/moi-00148>, 2024.
- 581 De Szoeké, R. A. and Levine, M. D.: The advective flux of heat by mean geostrophic motions in the Southern Ocean,
 582 *Deep-Sea Res. Part A Oceanogr. Res. Pap.*, 28(10), 1057–1085, [https://doi.org/10.1016/0198-0149\(81\)90048-0](https://doi.org/10.1016/0198-0149(81)90048-0),
 583 1981.
- 584 Dong, D., Brandt, P., Chang, P., Schütte, F., Yang, X., Yan, J., and Zeng, J.: Mesoscale eddies in the northwestern Pacific
 585 Ocean: three-dimensional eddy structures and heat/salt transports, *J. Geophys. Res. Oceans.*, 122, 9795–9813,
 586 <https://doi.org/10.1002/2017JC013303>, 2017.
- 587 Duan, Y., Liu, H., Yu, W., and Hou, Y.: Eddy properties in the Pacific sector of the Southern Ocean from satellite
 588 altimetry data, *Acta Oceanol. Sin.*, 35, 28–34, <https://doi.org/10.1007/s13131-016-0946-2>, 2016.
- 589 Duan, M., Ashford, J. R., Bestley, S., Wei, X. Y., Walters, A., and Zhu, G. P.: Otolith chemistry of *Electrona antarctica*
 590 suggests a potential population marker distinguishing the southern Kerguelen Plateau from the eastward-flowing
 591 Antarctic Circumpolar Current, *Limnol. Oceanogr.*, 62(2), 405–421, <https://doi.org/10.1002/lno.11612>, 2020.
- 592 Falkowski, P. G., Ziemann, D., Kolber, Z., and Bienfang, P. K.: Role of eddy pumping in enhancing primary production
 593 in the ocean, *Nature.*, 352, 55–58, <https://doi.org/10.1038/352055a0>, 1991.

- 594 Foppert, A., Donohue, K. A., Watts, D. R., and Tracey, K. L.: Eddy heat flux across the Antarctic Circumpolar Current
595 estimated from sea surface height standard deviation, *J. Geophys. Res. Oceans.*, 122(8), 6947–6964,
596 <https://doi.org/10.1002/2017JC012837>, 2017.
- 597 Frenger, I., Münnich, M., Gruber, N., and Knutti, R.: Southern Ocean eddy phenomenology, *J. Geophys. Res. Oceans.*,
598 120(11), 7413–7449, <https://doi.org/10.1002/2015JC011047>, 2015.
- 599 Fu, G., Yang, Y., Liang, X. S., and Zhao, Y.: Characteristics and dynamics of the interannual eddy kinetic energy
600 variation in the central Pacific sector of the Southern Ocean, *J. Geophys. Res. Oceans.*, 128, e2022JC019618,
601 <https://doi.org/10.1029/2022JC019618>, 2023.
- 602 Gille, S. T.: Mean sea surface height of the Antarctic Circumpolar Current from Geosat data: method and application, *J.*
603 *Geophys. Res. Oceans.*, 99(C9), 18255–18273, <https://doi.org/10.1029/94JC01172>, 1994.
- 604 Hallberg, R., and Gnanadesikan, A.: An Exploration of the Role of Transient Eddies in Determining the Transp
605 ort of a Zonally Reentrant Current, *J. Phys. Oceanogr.*, 31, 3312–3330. [https://doi.org/10.1175/1520-0485](https://doi.org/10.1175/1520-0485(2001)031%3C3312:AEOTRO%3E2.0.CO;2)
606 [https://doi.org/10.1175/1520-0485\(2001\)031%3C3312:AEOTRO%3E2.0.CO;2](https://doi.org/10.1175/1520-0485(2001)031%3C3312:AEOTRO%3E2.0.CO;2), 2001.
- 607 Hallberg, R., and Gnanadesikan, A.: The Role of Eddies in Determining the Structure and Response of the Wind-Driven
608 Southern Hemisphere Overturning: Results from the Modeling Eddies in the Southern Ocean (MESO) Project, *J.*
609 *Phys. Oceanogr.*, 36(12), 2232–2252, <https://doi.org/10.1175/JPO2980.1>, 2006.
- 610 He, Q., Zhan, W., Cai, S., Du, Y., Chen, Z., Tang, S., and Zhan, H.: Enhancing impacts of mesoscale eddies on Southern
611 Ocean temperature variability and extremes, *Proc. Natl. Acad. Sci. U.S.A.*, 120, e2302292120,
612 <https://doi.org/10.1073/pnas.2302292120>, 2023.
- 613 Henson, S. A. and Thomas, A. C.: A census of oceanic anticyclonic eddies in the Gulf of Alaska, *Deep-Sea Res. Part. I.*,
614 55, 163–176, <https://doi.org/10.1016/j.dsr.2007.11.005>, 2008.
- 615 Herraiz-Borreguero, L. and Rintoul, S. R.: Subantarctic mode water: distribution and circulation, *Ocean Dynamics*, 61,
616 103–126, doi:10.1007/s10236-010-0352-9, 2011.
- 617 Hogg, A. M., Meredith, M. P., Chambers, D. P., Abrahamsen, E. P., Hughes, C. W., and Morrison, A. K.: Recent trends in
618 the Southern Ocean eddy field, *J. Geophys. Res. Oceans.*, 120, 257–267, <https://doi.org/10.1002/2014JC010470>,
619 2015.
- 620 Holte, J. W., Talley, L. D., Chereskin, T. K., and Sloyan, B. M.: Subantarctic mode water in the southeast Pacific: effect
621 of exchange across the Subantarctic Front, *J. Geophys. Res. Oceans.*, 118, 2052–2066,
622 <https://doi.org/10.1002/jgrc.20144>, 2013.
- 623 Hughes, C. W.: Rossby waves in the Southern Ocean: a comparison of TOPEX/POSEIDON altimetry with model
624 predictions, *J. Geophys. Res. Oceans.*, 100, 15933–15950, <https://doi.org/10.1029/95JC01380>, 1995.
- 625 Hughes, C. W. and Ash, E. R.: Eddy forcing of the mean flow in the Southern Ocean, *J. Geophys. Res. Oceans.*, 106,
626 2713–2722, <https://doi.org/10.1029/2000JC900332>, 2001.
- 627 Isern-Fontanet, J., García-Ladona, E., and Font, J.: Vortices of the Mediterranean Sea: an altimetric perspective, *J. Phys.*
628 *Oceanogr.*, 36, 87–103, <https://doi.org/10.1175/JPO2826.1>, 2006.
- 629 Jan, S., Mensah, V., Andres, M., Chang, M.-H., and Yang, Y. J.: Eddy–Kuroshio interactions: local and remote effects, *J.*
630 *Geophys. Res. Oceans.*, 122, 9744–9764, <https://doi.org/10.1002/2017JC013476>, 2017.
- 631 Kim, Y. S. and Orsi, A. H.: On the variability of Antarctic Circumpolar Current fronts inferred from 1992–2011 altimetry,
632 *J. Phys. Oceanogr.*, 44, 3054–3071, <https://doi.org/10.1175/JPO-D-13-0217.1>, 2014.
- 633 Li, Z., England, M. H., Groeskamp, S., Cerovečki, I., and Luo, Y.: The Origin and Fate of Subantarctic Mode Water in
634 the Southern Ocean, *J. Phys. Oceanogr.*, 51(9), 2951–2972, doi:10.1175/JPO-D-20-0174.1, 2021.
- 635 Li, Z., Groeskamp, S., Cerovečki, I., and England, M. H.: The origin and fate of Antarctic Intermediate Water in the
636 Southern Ocean, *J. Phys. Oceanogr.*, 52, 2873–2890, <https://doi.org/10.1175/JPO-D-21-0221.1>, 2022.
- 637 Matsuoka, D., Araki, F., Inoue, Y., and Sasaki, H.: A new approach to ocean eddy detection, tracking, and event

- 638 visualization – application to the northwest Pacific Ocean, *Procedia Comput. Sci.*, 80, 1601–1611,
639 <https://doi.org/10.1016/j.procs.2016.05.491>, 2016.
- 640 Menna, M., Cotroneo, Y., Falco, P., Zambianchi, E., Di Lemma, R., Poulain, P.-M., Fusco, G., and Budillon, G.:
641 Response of the Pacific sector of the Southern Ocean to wind stress variability from 1995 to 2017, *J. Geophys.*
642 *Res. Oceans.*, 125, e2019JC015696, <https://doi.org/10.1029/2019JC015696>, 2020.
- 643 Moreau, S., Della Penna, A., Llort, J., Patel, R., Langlais, C., Boyd, P. W., Matear, R. J., Phillips, H. E., Trull, T. W.,
644 Tilbrook, B., Lenton, A., and Strutton, P. G.: Eddy-induced carbon transport across the Antarctic Circumpolar
645 Current, *Glob. Biogeochem. Cycles.*, 31, 1368–1386, <https://doi.org/10.1002/2017GB005669>, 2017.
- 646 Morrow, R., Church, J., Coleman, R., Chelton, D., and White, N.: Eddy momentum flux and its contribution to the
647 Southern Ocean momentum balance, *Nature.*, 357, 482–484, <https://doi.org/10.1038/357482a0>, 1992.
- 648 Morrow, R., Coleman, R., Church, J., and Chelton, D.: Surface eddy momentum flux and velocity variances in the
649 Southern Ocean from Geosat altimetry, *J. Phys. Oceanogr.*, 24, 2050–2071,
650 [https://doi.org/10.1175/1520-0485\(1994\)024<2050:SEMFV>2.0.CO;2](https://doi.org/10.1175/1520-0485(1994)024<2050:SEMFV>2.0.CO;2) 1994.
- 651 Morrow, R., Ward, M. L., Hogg, A. M., and Pasquet, S.: Eddy response to Southern Ocean climate modes, *J. Geophys.*
652 *Res. Oceans.*, 115, C10030, <https://doi.org/10.1029/2009JC005894>, 2010.
- 653 Naveira Garabato, A. C., Ferrari, R., and Polzin, K. L.: Eddy stirring in the Southern Ocean, *J. Geophys. Res.*, 116,
654 C09017, <https://doi.org/10.1029/2010JC006818>, 2011.
- 655 Naveira Garabato, A. C., Heywood, K. J., and Stevens, D. P.: Modification and pathways of Southern Ocean Deep Waters
656 in the Scotia Sea, *Deep-Sea Res. Part I.*, 49, 681–705, [https://doi.org/10.1016/S0967-0637\(01\)00071-1](https://doi.org/10.1016/S0967-0637(01)00071-1), 2002.
- 657 Okubo, A.: Horizontal dispersion of floatable particles in the vicinity of velocity singularities such as convergences,
658 *Deep-Sea Res. Oceanogr. Abstr.*, 17, 445–454, [https://doi.org/10.1016/0011-7471\(70\)90059-8](https://doi.org/10.1016/0011-7471(70)90059-8), 1970.
- 659 Orsi, A. H., Whitworth, T., and Nowlin, W. D.: On the meridional extent and fronts of the Antarctic Circumpolar Current,
660 *Deep-Sea Res. Part I.*, 42, 641–673, [https://doi.org/10.1016/0967-0637\(95\)00021-W](https://doi.org/10.1016/0967-0637(95)00021-W), 1995.
- 661 Park, Y.-H., Gamberoni, L., and Charriaud, E.: Frontal structure, water masses, and circulation in the Crozet Basin, *J.*
662 *Geophys. Res.*, 98, 12361–12385, <https://doi.org/10.1029/93JC00938>, 1993.
- 663 Park, Y.-H., Park, T., Kim, T.-W., Lee, S.-H., Hong, C.-S., Lee, J.-H., Rio, M.-H., Pujol, M.-I., Ballarotta, M., Durand, I.,
664 and Provost, C.: Observations of the Antarctic Circumpolar Current over the Udintsev Fracture Zone, the
665 narrowest choke point in the Southern Ocean, *J. Geophys. Res. Oceans.*, 124,
666 4511–4528, <https://doi.org/10.1029/2019JC015024>, 2019.
- 667 Patel, R. S., Phillips, H. E., Strutton, P. G., Lenton, A., and Llort, J.: Meridional heat and salt transport across the
668 Subantarctic Front by cold-core eddies, *J. Geophys. Res. Oceans.*, 124, 981–1004,
669 <https://doi.org/10.1029/2018JC014655>, 2019.
- 670 Pujol, M.-I. and Grassi, K.: Product user manual for sea level altimeter products:
671 SEALEVEL_GLO_PHY_L4_NRT_008_046, SEALEVEL_EUR_PHY_L4_NRT_008_060,
672 SEALEVEL_GLO_PHY_L4_MY_008_067, SEALEVEL_EUR_PHY_L4_MY_008_068, Issue 1.0,
673 Copernicus Marine Environment Monitoring Service
674 (CMEMS), [https://catalogue.marine.copernicus.eu/documents/PUM/CMEMS-SL-PUM-008-046-047-060-068.p](https://catalogue.marine.copernicus.eu/documents/PUM/CMEMS-SL-PUM-008-046-047-060-068.pdf)
675 [df](https://catalogue.marine.copernicus.eu/documents/PUM/CMEMS-SL-PUM-008-046-047-060-068.pdf), 2025.
- 676 Qiu, C., Yang, Z., Feng, M., Yang, J., Rippeth, T. P., Shang, X., Sun, Z., Jing, C., and Wang, D.: Observational energy
677 transfers of a spiral cold filament within an anticyclonic eddy, *Prog. Oceanogr.*, 220, 103187,
678 <https://doi.org/10.1016/j.pocean.2023.103187>, 2024.
- 679 Sallée, J.-B., Speer, K., and Morrow, R.: Southern Ocean fronts and their variability to climate modes, *J. Climate.*, 21,
680 3020–3039, 2008.
- 681 Saunders, R. A., Collins, M. A., Stowasser, G., and Tarling, G. A.: Southern Ocean mesopelagic fish communities in the

- 682 Scotia Sea are sustained by mass immigration, *Mar. Ecol. Prog. Ser.*, 569, 173–185,
683 <https://doi.org/10.3354/meps12093>, 2017.
- 684 Saraceno, M. and Provost, C.: On eddy polarity distribution in the southwestern Atlantic, *Deep Sea Research Part I: Oceanographic Research Papers*, 69, 62–69, doi:10.1016/j.dsr.2012.07.001, 2012.
- 685
- 686 Shi, F., Shi, Q., Luo, Y. Y., Wu, R. H., Yang, Q. H., Liu, J. P., Yang, J., and Song, J.: Meridional shift of Southern Ocean
687 mesoscale eddies since the 1990s, *Adv. Atmos. Sci.*, 42, 1–10, <https://doi.org/10.1007/s00376-024-4249-9>,
688 2025.
- 689 Shi, J. R., Talley, L. D., Xie, S. P., Peng, Q., and Liu, W.: Ocean warming and accelerating Southern Ocean zonal flow,
690 *Nat. Clim. Chang.*, 11, 1090–1097, <https://doi.org/10.1038/s41558-021-01212-5>, 2021.
- 691 Sokolov, S. and Rintoul, S. R.: Structure of Southern Ocean fronts at 140°E, *J. Mar. Syst.*, 37, 151–184,
692 [https://doi.org/10.1016/S0924-7963\(02\)00200-2](https://doi.org/10.1016/S0924-7963(02)00200-2), 2002.
- 693 Sokolov, S. and Rintoul, S. R.: On the relationship between fronts of the Antarctic Circumpolar Current and surface
694 chlorophyll concentrations in the Southern Ocean, *J. Geophys. Res. Oceans.*, 112, C07030,
695 <https://doi.org/10.1029/2006JC004072>, 2007.
- 696 Sprintall, J.: Seasonal to interannual upper-ocean variability in the Drake Passage, *J. Mar. Res.*, 61, 27–57,
697 <https://doi.org/10.1357/002224003321586408>, 2003.
- 698 Straub, D. N.: On the transport and angular momentum balance of channel models of the Antarctic Circumpolar Current,
699 *J. Phys. Oceanogr.*, 23, 776–782, [https://doi.org/10.1175/1520-0485\(1993\)023<0776:OTTAAM>2.0.CO;2](https://doi.org/10.1175/1520-0485(1993)023<0776:OTTAAM>2.0.CO;2),
700 1993.
- 701 Swart, N. C., Ansorge, I. J., and Lutjeharms, J. R. E.: Detailed characterization of a cold Antarctic eddy, *J. Geophys. Res. Oceans.*, 113, C01009, <https://doi.org/10.1029/2007JC004190>, 2008.
- 702
- 703 Thompson, A. F., Haynes, P. H., Wilson, C., and Richards, K. J.: Rapid Southern Ocean front transitions in an
704 eddy-resolving ocean GCM, *Geophys. Res. Lett.*, 37, L23602, <https://doi.org/10.1029/2010GL045386>, 2010.
- 705 Thompson, A. F. and Sallée, J.-B.: Jets and topography: Jet transitions and the impact on transport in the Antarctic
706 Circumpolar Current, *J. Phys. Oceanogr.*, 42, 956–972, <https://doi.org/10.1175/JPO-D-11-0135.1>, 2012.
- 707 Thorpe, S. E., Heywood, K. J., Brandon, M. A., and Stevens, D. P.: Variability of the southern Antarctic Circumpolar
708 Current front north of South Georgia, *J. Mar. Syst.*, 37, 87–105, [https://doi.org/10.1016/S0924-7963\(02\)00197-5](https://doi.org/10.1016/S0924-7963(02)00197-5),
709 2002.
- 710 Valla, D., Piola, A. R., Meinen, C. S., and Campos, E.: Strong mixing and recirculation in the northwestern Argentine
711 Basin, *J. Geophys. Res. Oceans.*, 123, 4624–4648, <https://doi.org/10.1029/2018JC013907>, 2018.
- 712 Vereshchaka, A., Musaeva, E., and Lunina, A.: Biogeography of the Southern Ocean: environmental factors driving
713 mesoplankton distribution south of Africa, *PeerJ.*, 9, e11411, [10.7717/peerj.11411](https://doi.org/10.7717/peerj.11411), 2021.
- 714 Weiss, J.: The dynamics of enstrophy transfer in two-dimensional hydrodynamics, *Physica D.*, 48, 273–294,
715 [https://doi.org/10.1016/0167-2789\(91\)90088-Q](https://doi.org/10.1016/0167-2789(91)90088-Q), 1991.
- 716 Xia, X., Hong, Y., Du, Y., and Xiu, P.: Three types of Antarctic Intermediate Water revealed by a machine learning
717 approach, *Geophys. Res. Lett.*, 49, e2022GL099445, <https://doi.org/10.1029/2022GL099445>, 2022.
- 718 Zhang, Y., Chambers, D., and Liang, X.: Regional trends in Southern Ocean eddy kinetic energy, *J. Geophys. Res. Oceans.*, 126, e2020JC016986, [10.1029/2020JC016973](https://doi.org/10.1029/2020JC016973), 2021.
- 719
- 720 Zhu, G. P., Qian, H. R., Wei, L., Fach, B. A., Bestley, S., Yan, C. B., and Ashford, J. R.: Otolith chemistry indicates
721 structuring of the Subantarctic myctophid *Electrona carlsbergi* in the Antarctic Circumpolar Current and
722 Antarctic Slope Current off the South Shetland Islands, *Palaeogeogr. Palaeoclimatol. Palaeoecol.*, 675, 113062,
723 <https://doi.org/10.1016/j.palaeo.2025.113062>, 2025.